Paul Wilbur

NASA CR - 135047


# CUSPED MAGNETIC FIELD MERCURY ION THRUSTER

PREPARED FOR

LEWIS RESEARCH CENTER

NATIONAL AERONAUTICS AND SPACE ADMINSTRATION

Grant NGR-06-002-112

by

John R. Beattie

Approved by

Paul J. Wilbur

July 1976

Department of Mechanical Engineering

Colorado State University

Fort Collins, Colorado

| 1. Report No. | 2. Government Accession No. | 3. Recipient's Catalog No. |
|---|---|---|
| NASA CR - 135047 | | |

| 4. Title and Subtitle | 5. Report Date |
|---|---|
| CUSPED MAGNETIC FIELD MERCURY ION THRUSTER | July, 1976 |
| | 6. Performing Organization Code |

| 7. Author(s) | 8. Performing Organization Report No. |
|---|---|
| John R. Beattie and Paul J. Wilbur | |
| | 10. Work Unit No. |

| 9. Performing Organization Name and Address | 11. Contract or Grant No. |
|---|---|
| Department of Mechanical Engineering<br>Colorado State University<br>Fort Collins, Colorado 80523 | NGR-06-002-112 |
| | 13. Type of Report and Period Covered |

| 12. Sponsoring Agency Name and Address | 14. Sponsoring Agency Code |
|---|---|
| National Aeronautics and Space Administration<br>Washington, D. C. 20546 | |

15. Supplementary Notes Grant Monitor - William Kerslake, NASA Lewis Research Center, Cleveland, Ohio 44135.

This report is a reproduction of the Ph.D. Thesis of John R. Beattie. It is submitted to the sponsor and to the distribution list in this form both as a presentation of the technical material, and as an indication of the academic program supported by this Grant.

16. Abstract

The importance of a uniform current density profile in the exhaust beam of an electrostatic ion thruster is discussed in terms of thrust level and accelerator system lifetime. A residence time approach is used to explain the nonuniform beam current density profile of the SERT II divergent magnetic field thruster and to propose a magnetic field modification (the cusped magnetic field geometry) which should produce a highly uniform beam profile. A discharge chamber model is proposed and mathematical expressions are derived which relate the thruster discharge power loss, propellant utilization, and double-to-single ion density ratio to the geometry and plasma properties of the discharge chamber. These relationships are applied to a cylindrical discharge chamber model of the SERT II thruster and suggest that, in addition to the magnetic field modification, the discharge chamber length of this thruster should be reduced. These modifications should result in a thruster having a highly uniform beam profile, good performance, and a low double ion population.

Experimental results are presented for a wide range of the discharge chamber length. The thruster designed for this investigation was operated with a cusped magnetic field as well as a divergent field geometry, and the cusped field geometry is shown to be superior from the standpoint of beam profile uniformity, performance, and double ion population. Beam profile measurements 6 mm downstream of the accelerator grid indicate the beam profile flatness parameter (which quantitatively describes the uniformity of the profile) is 0.7, and throttled thruster operation results in a beam flatness parameter of 0.82. At about the same thrust and performance levels, the beam flatness parameter of the cusped field thruster is 40 percent higher than the SERT II thruster value. This implies a 40 percent increase in the accelerator system lifetime due to a reduction in localized erosion of the accelerator grid caused by the impingement of charge-exchange ions.

| 17. Key Words (Suggested by Author(s)) | 18. Distribution Statement |
|---|---|
| Electrostatic Thruster | Unclassified - Unlimited |

| 19. Security Classif. (of this report) | 20. Security Classif. (of this page) | 21. No. of Pages | 22. Price* |
|---|---|---|---|
| Unclassified | Unclassified | 108 | |

* For sale by the National Technical Information Service, Springfield, Virginia 22161

TABLE OF CONTENTS

LIST OF FIGURES

LIST OF FIGURES - Continued

LIST OF FIGURES - Continued

# I. INTRODUCTION

Propelling space vehicles by electrical means was proposed as early as 1906 by Robert H. Goddard [1], and since that time numerous electric space propulsion concepts have been introduced [1,2]. Among these proposals the electrostatic acceleration of positive ions is generally considered the most promising for high-impulse space missions. In particular, the electron-bombardment ion thruster introduced in 1960 [3,4] remains today the most likely choice for primary and many auxiliary space propulsion needs [5]. A discussion of the historical development and current technology status of electron-bombardment ion thrusters can be found in the literature [5,8].

## Thruster Lifetime

The low-thrust nature of electron-bombardment ion thrusters requires long mission times to achieve the desired spacecraft velocity increment. This requirement dictates thruster designs which can operate for extended periods of time; perhaps as long as 20,000 hours [9,10]. Designing thrusters to operate for such long mission times poses many unique and challenging problems for the designer and requires life-testing of critical thruster components under simulated space conditions. The operational lifetime of a thruster is usually determined by the failure of one of its components rather than failure of the thruster as a whole. However, in some instances an early failure may be due to an

interaction between two or more components which individually had much longer lifetimes. For example, both thrusters aboard the SERT II spacecraft, which was launched in 1970 [11], failed as a result of electrical shorts in the accelerator system. The cause of the failure was due not to poor accelerator system design but to the close proximity of the accelerator grid and the neutralizer cathode assembly. Low-energy ions created by the neutralizer discharge were accelerated to the downstream side of the accelerator grid resulting in localized sputtering. Metallic fragments produced by the erosion process eventually became lodged between the screen and accelerator grids resulting in an electrical short. The problem has since been eliminated simply by relocating the neutralizer cathode.

The extension of the electron-bombardment thruster lifetime from the 100 or so hours of the earliest designs to around 10,000 hours for the more recent designs [12] has involved a somewhat systematic process of prolonging the life of individual components. During a development program the same thruster component may emerge periodically as the lifetime limitation. An example is the accelerator system which, as discussed earlier, failed and caused the termination of the SERT II mission. The source of this failure was easily conjectured from the results of subsequent ground tests, and a simple solution was identified and incorporated into current thruster designs. There are, however, additional accelerator system erosion phenomena which are recognized today as posing potential life limitations: (1) erosion of the accelerator grid caused by charge exchange impingement, (2) accelerator grid erosion caused by direct ion impingement, and (3) erosion of the screen grid as a result of bombardment by doubly charged ions.

Charge-exchange ions are produced when an ion and neutral passing through the accelerator system exchange identity. This process occurs when an electron leaves the slow neutral and attaches itself to the fast ion. The mercury* charge-exchange cross section is about $6 \times 10^{-19} m^2$ for the ion energy range of interest to electric propulsion, and this is by far the largest of any of the cross sections associated with the reactions occurring during thruster operation. The products of the charge-exchange reaction are a fast neutral and slow ion, and if the reaction occurs near the negative accelerator grid the low-energy ion will be accelerated toward the grid and upon impact may cause considerable sputtering damage. The severity of the problem is illustrated in Figure 1 which shows the charge-exchange erosion pattern observed on the downstream side of an accelerator grid after having been operated for about 3,000 hours. Deep triangular pits are formed in the regions surrounded by three adjacent holes where the impinging current density is highest. Although these deep pits are first to erode completely through, failure of the accelerator grid results from the eventual breakthrough of the shallower troughs in the regions adjacent to two holes. The upstream side of the accelerator grid also undergoes charge-exchange erosion; but at a much lower rate.

Direct ion impingement upon the accelerator grid (as opposed to charge-exchange ion impingement) may result during thruster operation at high plasma density conditions. Under these conditions the plasma sheath tends to penetrate the screen grid holes and assumes a curvature

---

*Mercury is generally chosen as a propellant because of its low ionization potential, high molecular weight, and ease in handling and storing.

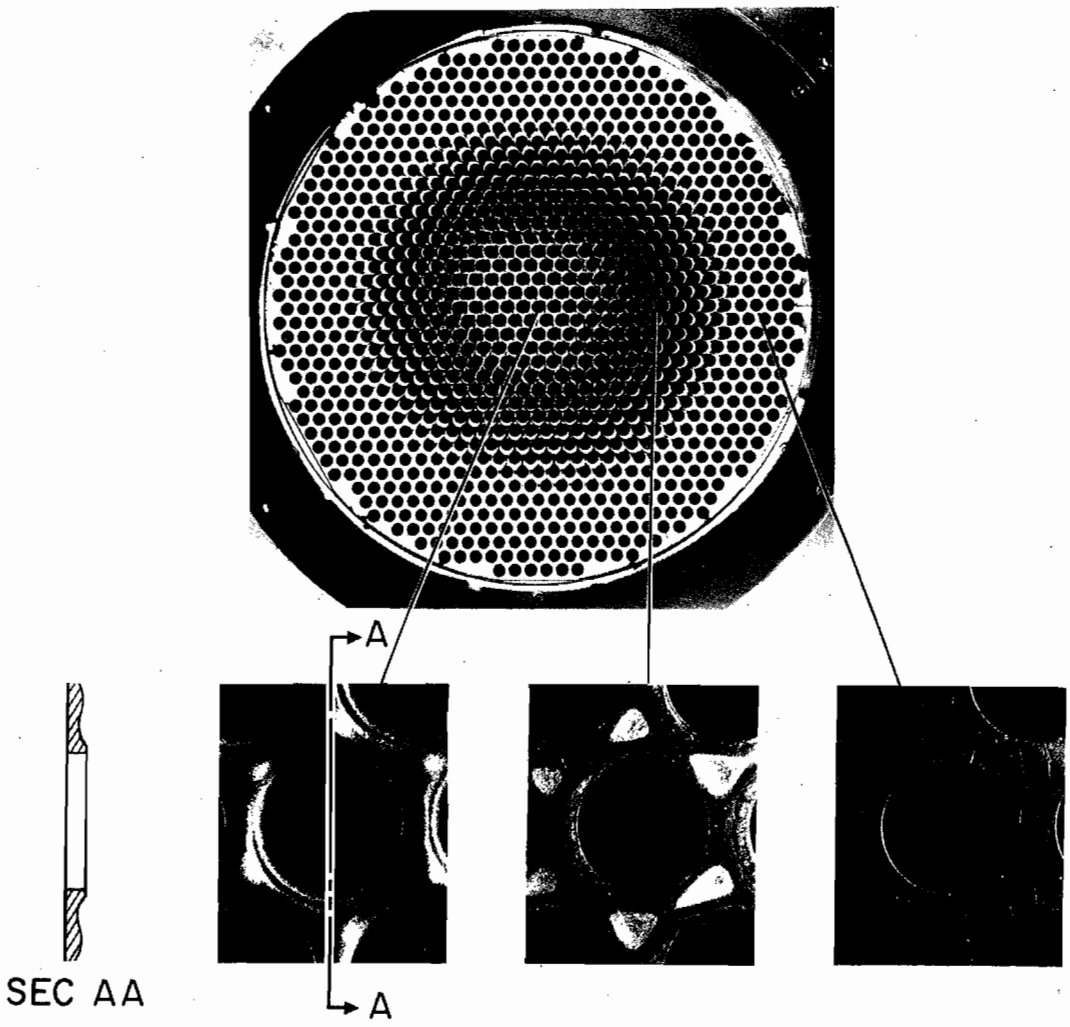


Figure 1. Charge-exchange ion erosion pattern on the downstream side of an accelerator grid. (Photo courtesy of Hughes Research Laboratories, Malibu, California.)

which can direct plasma ions into trajectories terminating on the accelerator grid. Low plasma density operation can also cause direct ion impingement as a result of crossover trajectories. Crossover occurs when the plasma sheath recedes away from the screen grid aperture and assumes a highly concave geometry which tends to focus ions along trajectories which cross over the axis of the hole. The low-density region near the chamber wall can also cause direct ion impingement when the plasma sheath moves upstream to compensate for the reduction in plasma density and assumes a nonsymmetrical shape which directs ions onto one side of the accelerator grid hole. Due to the nonuniform plasma density profile which exists inside most discharge chambers, the first effect tends to occur in the center of the chamber where the plasma density is high while the other two effects occur near the edge of the chamber where the plasma density is lower.

Screen grid erosion due to the impingement of doubly charged ions may also represent a lifetime limit on accelerator systems. Although the ion energy is considerably less than in the case of charge exchange and direct impingement, the amount of material available for erosion is substantially reduced also. This is because good thruster performance requires thin screen grids to minimize recombination losses and thick accelerator grids to minimize neutral particle loss. The long-term effects of double ion erosion can be serious [13], and perhaps the best approach to eliminating this problem is to reduce the number, as well as the energy, of the double ions present in the discharge chamber. Substantial progress in this area has been realized recently by use of small-hole accelerator grids [14]. These electrodes have accelerator

holes which are only about one-half the diameter of the screen grid hole and, at the same propellant flow rate, result in a higher neutral density within the discharge chamber. This allows efficient operation at much lower discharge voltage levels which results in a reduction in double ion production rate and particle energy.

## Present Investigation

The specific objective of the present investigation is to increase the accelerator grid lifetime by reducing local charge-exchange ion erosion. The most direct approach to the problem is to reduce the rate of production of charge-exchange ions. Some insight into how this might be accomplished can be gained by considering the expression for the accelerator grid charge-exchange current

$$I_{CE} = n_o j_B \sigma_{CE} V \tag{1}$$

where $I_{CE}$ = accelerator grid charge-exchange current
$n_o$ = neutral particle density
$j_B$ = beam current density
$\sigma_{CE}$ = charge-exchange cross section
$V$ = charge-exchange ion production volume

The charge-exchange cross section $\sigma_{CE}$ is determined by the choice of propellant and the optimum specific impulse for the mission, while the volume V is determined by the accelerator system design parameters (grid spacing and thickness, location of the neutralization plane, and beamlet diameter). Therefore, for a given accelerator system the only

other variables remaining which are at the designers disposal are the neutral density and beam current density. For a given propellant flow rate the beam current density is proportional to the propellant utilization* $\eta_u$, and the neutral density is proportional to the quantity $1 - \eta_u$. The charge-exchange current can thus be expressed as a simple proportionality

$$I_{CE} \propto \eta_u(1 - \eta_u) \tag{2}$$

From this expression one can see that the charge-exchange current is zero when the propellant utilization is either zero or unity. The former case corresponds to all the propellant exiting the thruster in the unionized state and is of no interest to space propulsion. The latter case is unrealistic from physical considerations since a prohibitively large power supply would be required to ionize 100 percent of the propellant. This can be illustrated by considering a typical thruster performance curve presented in Figure 2. The performance parameter plotted as the ordinate is the discharge power loss, or the energy expended in producing a beam ion, and is calculated by use of the expression

$$P = \frac{I_{anode}V_{anode}}{I_{beam}} \tag{3}$$

*Propellant utilization is defined as the fraction of the total propellant flow rate which exits the thruster in the ionized state. This parameter is of great importance in the electric propulsion field since particles leaving the accelerator system as neutrals produce negligible thrust.

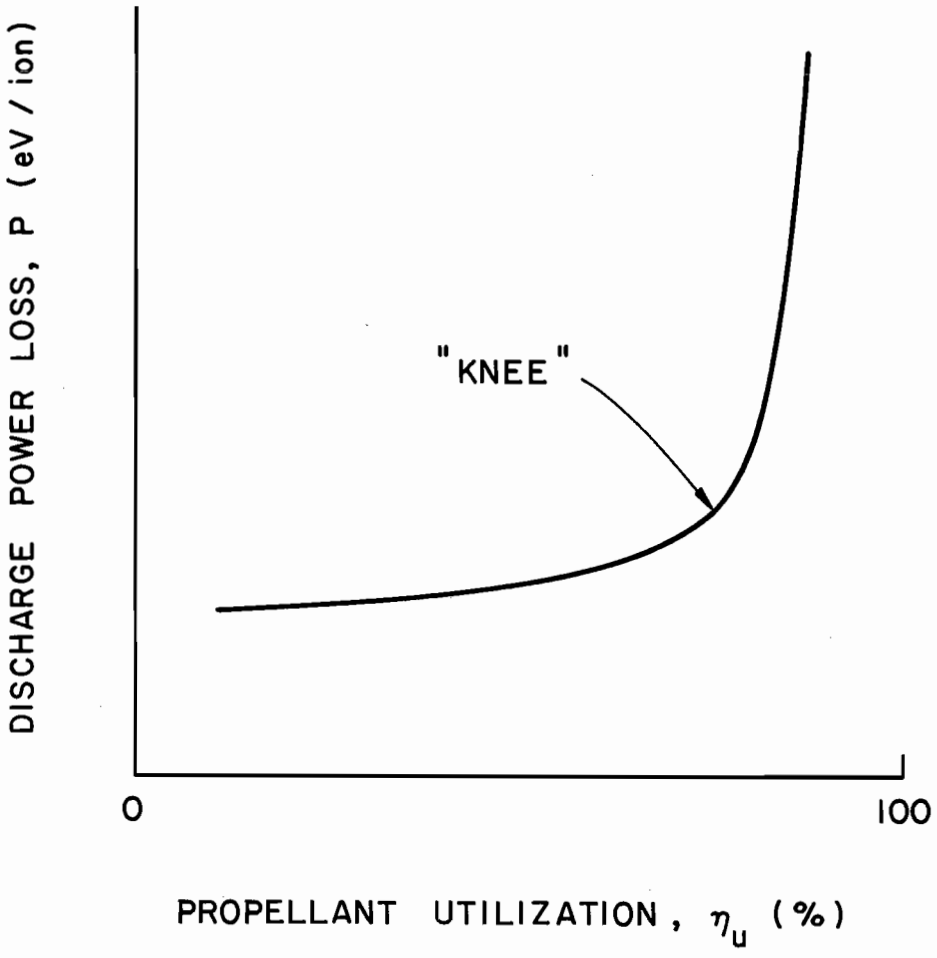


Figure 2. Typical thruster performance curve.

where $P$ = discharge power loss, eV/ion

$I_{anode}$ = anode current

$V_{anode}$ = anode potential

$I_{beam}$ = beam current

The bend in the performance curve is referred to as the "knee" of the curve and generally represents the optimum operating point. Operation to the right of the performance curve knee requires a substantial increase in power supply weight with a relatively small reduction in propellant weight. Operation to the left of the knee results in a substantial increase in propellant mass accompanied by only a slight decrease in power supply mass. Equation 2 indicates a higher charge-exchange current will generally result from thruster operation to the left of the knee.

At first glance it appears little can be done to reduce the charge-exchange ion production. However, closer examination of Figure 1 indicates the erosion damage is strongly dependent on the radial coordinate, and the erosion rate is greatest on the thruster centerline. Current density measurements in the thruster exhaust beam reveal the profile is quite peaked, and the maximum current density occurs on the beam centerline. These observations, along with the dependence of the charge-exchange current on the local beam current density as illustrated by Equation 1, explain the radial variation of the charge-exchange erosion. A quantity which describes the nonuniformity of the beam current density profile is the flatness parameter F which is defined as the ratio of average-to-maximum beam current density.

Assuming the beam is axisymmetric the flatness parameter can be calculated by the relation

$$F = \frac{\int_0^R 2\pi r j(r) dr}{\pi R^2 j_{max}} \tag{4}$$

where F = beam flatness parameter

r = radial coordinate

R = beam radius

j = current density

Figure 3 presents an example of two beam profiles which have the same average current density. The uniform profile has a flatness parameter of 1.0, and the nonuniform profile (a cosine distribution) has a value of F equal to 0.46. This nonuniform profile is typical of state-of-the-art divergent field chamber designs and indicates the current density at the beam center is more than twice the value that would exist with a uniform profile having the same integrated current.

The dependence of the accelerator grid erosion rate on local beam current density suggests the grid (assumed to have homogeneous composition and thickness) will wear through first in regions where the current density is a maximum. Experimental measurements indicate the current density is a maximum on the beam centerline, and, thus, the wear rate pattern illustrated in Figure 1 is to be expected. These observations suggest an improvement in accelerator grid life could be realized by distributing the charge-exchange ion erosion more evenly

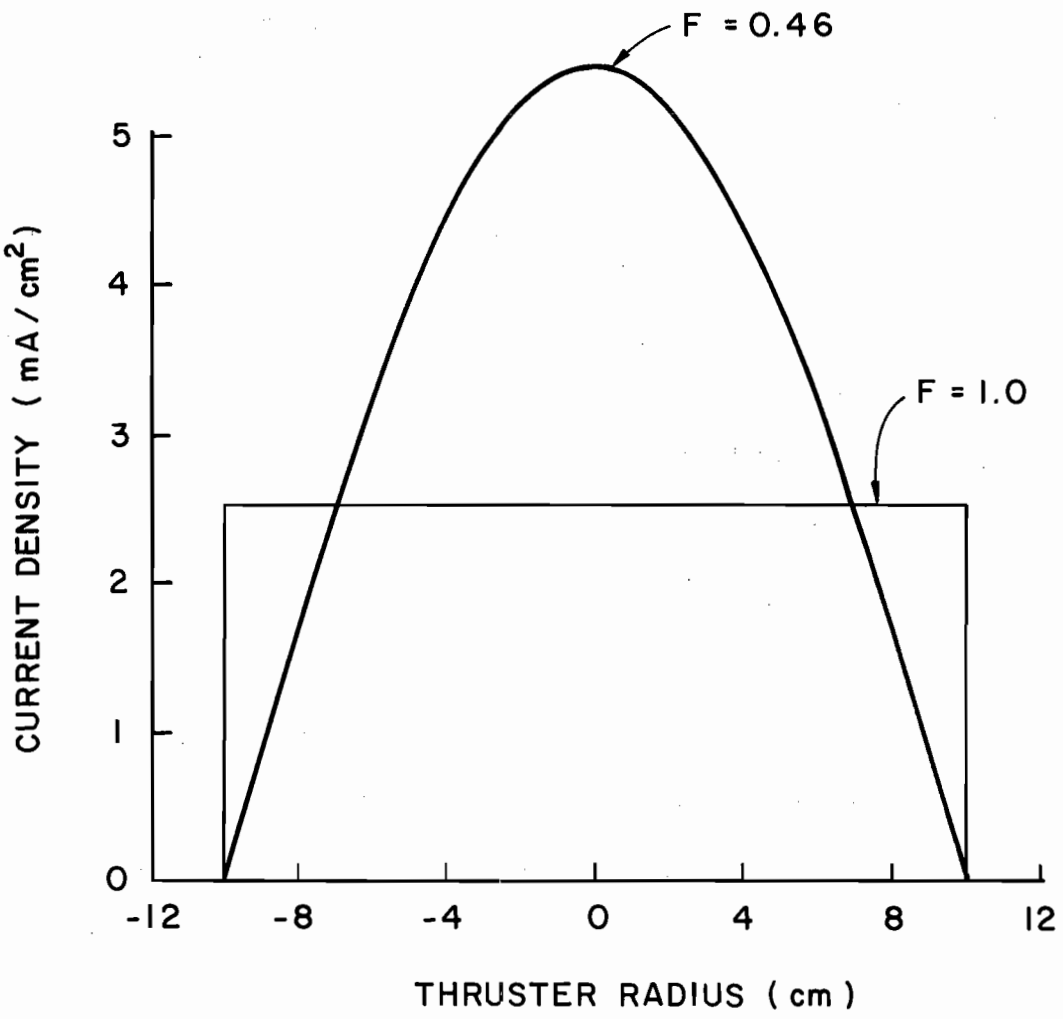


Figure 3. Beam current density profiles.

across the grid. The correlation between erosion and current density profiles suggests a more uniform erosion rate could be realized by increasing the beam flatness parameter.

An additional incentive for achieving a uniform current density profile can be illustrated by use of the thrust equation for an electrostatic accelerator

$$T = j_{ave} A (2mV^{+}/q)^{1/2} \tag{5}$$

where $T$ = thrust

$j_{ave}$ = average current density

$A$ = beam area

$V^{+}$ = net accelerating potential

$q/m$ = propellant charge-to-mass ratio

For a given propellant, exhaust velocity, and thruster diameter, the thrust equation reduces to a simple proportionality between thrust and average beam current density. By introducing the beam flatness parameter F, the proportionality can be written as

$$T \propto F j_{max} \tag{6}$$

Since the accelerator grid lifetime is determined by the maximum beam current density, Equation 6 indicates the thrust is directly proportional to beam flatness for a given accelerator grid lifetime. Uniform beam profiles are therefore seen to be highly desirable from the

standpoint of (1) increasing accelerator grid lifetime at a given thrust level by reducing localized charge-exchange ion erosion or (2) increasing the thrust level for a given accelerator grid lifetime. Either improvement is of interest to the thruster designer, and together they form the basis of this investigation.

Unless otherwise noted, SI (rationalized mks) units are used throughout this paper.

# II. DISCHARGE CHAMBER THEORY

A brief qualitative description of the operation of electron-bombardment ion thrusters is presented as the first part of this chapter. The plasma properties and operating parameters given are representative of mercury which was the propellant used in this investigation. A discussion of the thruster magnetic field geometry and its relationship to the shape of the beam current density profile is given in the second part of the chapter. The third section presents the application of a neutral residence time theory to a modern discharge chamber design and suggests a magnetic field modification which should produce a more uniform ion beam current density profile. The final sections discuss the effects this modification is expected to produce on thruster performance and the discharge chamber double ion content.

## Thruster Operation

Contemporary electron-bombardment ion thrusters consist of a cylindrical discharge chamber with a set of grids mounted at the downstream end as illustrated in Figure 4. The cylindrical chamber wall serves as the anode, and the upstream end of the chamber houses a hollow cathode [7]. The cathode is mounted within a soft-iron pole piece and is shielded from the bulk of the thruster discharge by use of a circular baffle. This divides the thruster into two discharge regions and provides sputter erosion protection for the hollow cathode.

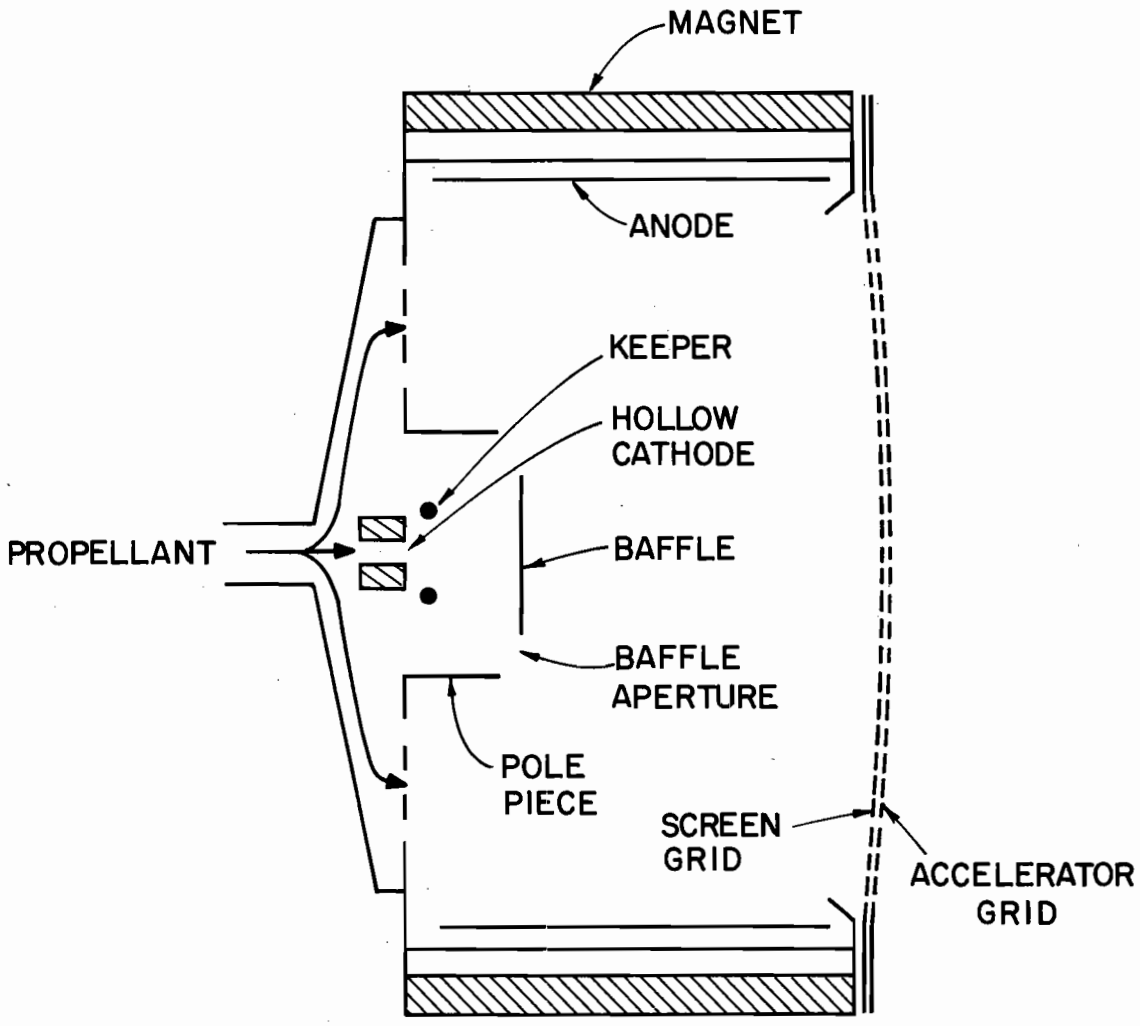


Figure 4. Electron-bombardment ion thruster.

Operational lifetimes on the order of 10,000 hours have been realized with this arrangement [15].

The ion accelerating system consists of two closely-spaced grids containing many small diameter holes. The grids have a slightly spherical shape which gives the desired stability under the thermal loading produced by temperature gradients in both the radial and axial directions. The screen grid has as large an open-area fraction as structural and fabrication considerations will permit. Usually this amounts to about a 70 percent open-area fraction which is sufficient to extract nearly all the ions reaching the accelerator system. In order to minimize ion recombination on the walls of the cylindrical holes, the screen grid is made as thin as structural and fabrication considerations will allow. The accelerator grid, on the other hand, usually has a low open-area fraction and can be much thicker, both of which help to minimize the loss of neutral particles. The extracted ion beam is current and space charge neutralized to eliminate spacecraft charging and space charge accumulation within the ion beam. Neutralization is achieved by the use of a hollow cathode neutralizer which is similar in design to the hollow cathode used inside the thruster.

During typical thruster operation with mercury propellant, up to 90-95 percent of the neutral gas is injected into the thruster at the upstream end of the discharge chamber. The remainder of the propellant enters through the hollow cathode. The neutral gas density near the accelerator system is of the order of $10^{18}$ $m^{-3}$ and is essentially independent of propellant flow rate at efficient operating conditions [6]. The low neutral density results in free-molecular flow of the

atomic species, and the neutrals acquire the mean chamber wall temperature of around 500 $^{o}$K.

Ionization of the neutral propellant atoms, which reside in the ground energy state and various excited states, is accomplished by electron impact involving two groups of ionizing electrons. The first group is comprised of the electrons which are accelerated from the hollow cathode into the main discharge region, and these electrons acquire an energy roughly equal to the difference in the plasma potentials of the two regions. The difference in potential is usually of the order of 30 V, and the high-energy electrons in this group are referred to as monoenergetic, or primary, electrons. The second group of electrons originates from the inelastic interactions of the primary electrons with neutrals and ions. These interactions reduce the energy of the primary electrons and release low-energy secondary electrons. The low-energy electrons rapidly randomize and approximate a Maxwellian distribution of energies characterized by a temperature of the order of 5 eV. The Maxwellian group usually contains 90-95 percent of the plasma electrons. However, this value can change with thruster size and geometry and is quite sensitive to thruster operating conditions. The remainder of the electrons are primaries which, although few in number, contribute a large percentage of the ionizations due to their higher energy.

During operation the propellant gas is only partially ionized, and an electron density of about $10^{17}$ $m^{-3}$ is typical. The relatively low electron temperature and high density results in a Debye length of $5 \times 10^{-5}$ m. The Debye number is about $6 \times 10^{4}$, and under these conditions the plasma may be considered quasi-neutral.

## Magnetic Field

The mean free path for electron-atom ionizing collisions is about 20 m for 30-40 eV electrons and a neutral density of $10^{18}$ $m^{-3}$. Since the path length is much greater than the thruster dimensions, a magnetic field is employed to prevent electrons from escaping to the anode without first encountering a neutral. Magnetic field strengths of about $5 \times 10^{-3}$ $W/m^2$ are typical of most electron-bombardment thrusters and result in an electron gyro radius of about $4 \times 10^{-3}$ m for 30 eV electrons. The ions, on the other hand, are essentially unaffected by the magnetic field due to their large mass.

The shape of the ion beam current density profile is highly influenced by the magnetic field geometry which exists inside the discharge chamber. This effect is illustrated in Figure 5 which indicates three different discharge chamber designs and their associated beam current density profiles. Studies using a divergent magnetic field geometry [16] have indicated a good statistical correlation exists between the shape of the beam current density profile at the accelerator grid and the ion number density profile near the screen grid. Similarly, a good qualitative correlation between the ion density and beam current density profiles was observed with the radial field thruster design [17].

The relationship between the magnetic field geometry and ion density profile can be explained on the basis of electron transport along, and transverse to, the magnetic field lines. In the axial magnetic field thruster illustrated in Figure 5a, the high-energy electrons are emitted by a refractory-metal cathode located on the thruster centerline. The emitted electrons have direct access to the

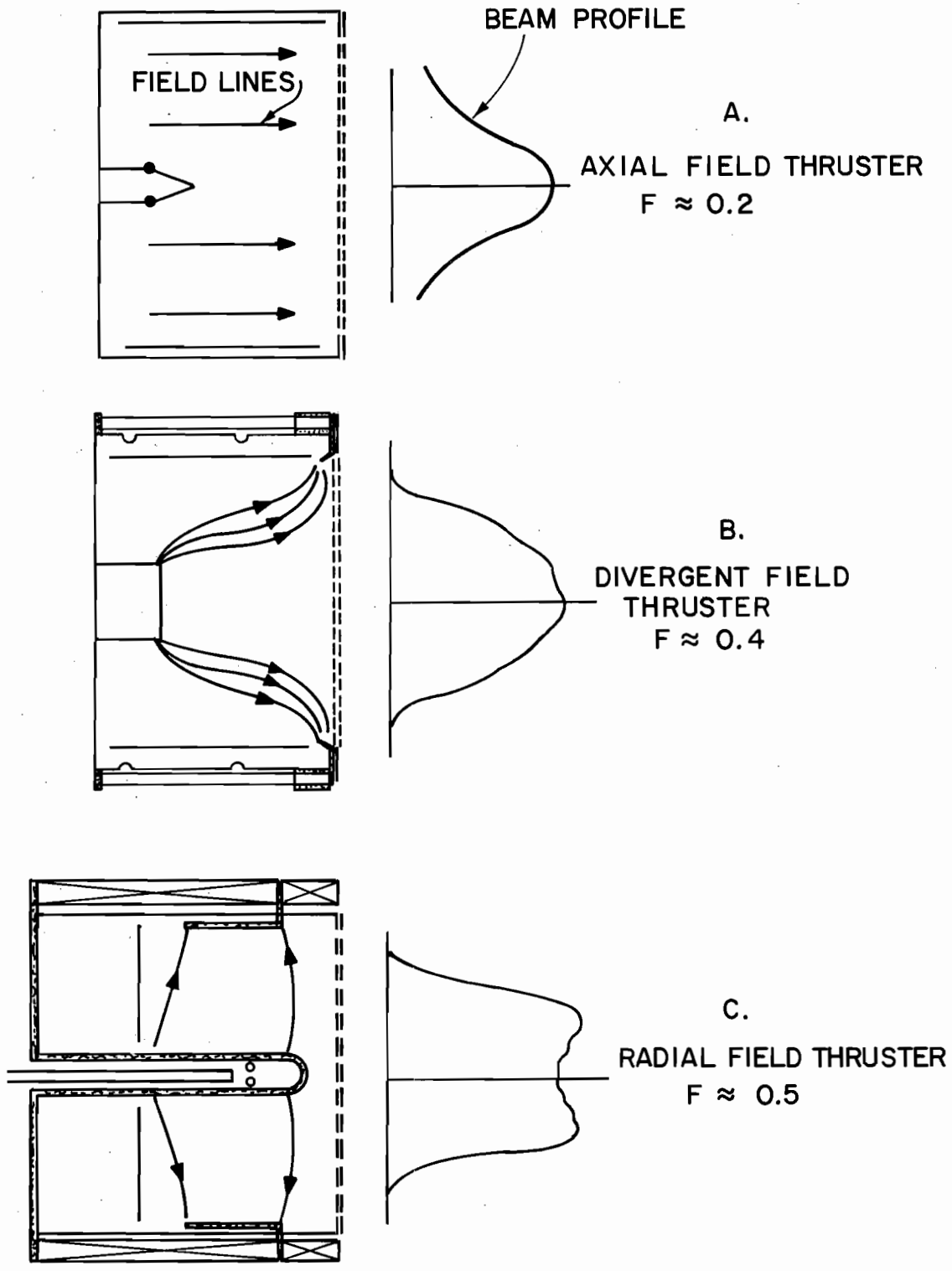


Figure 5. Axial, divergent, and radial field discharge chambers and their associated beam current density profiles.

central core of the chamber and reach the remainder of the chamber cross section by collisions with neutrals and, to a lesser extent, ions. The inelastic collisions with neutrals and ions results in primary electrons losing much of their energy. As a result the high-energy electrons are concentrated in the central core region, and the ion production rate and ion density decrease radially towards the anode.

The divergent magnetic field geometry illustrated in Figure 5b allows the energetic electrons access to the entire chamber cross section by traveling along the magnetic field lines which originate near the baffle aperture region. The primaries are no longer confined to the central portion of the chamber but have access to the entire bell-shaped region as illustrated in the figure. This region is known as the primary electron region, and the upstream boundary is called the "critical field line." The critical field line is defined as the innermost field line which intercepts the anode. The basis for this definition is simply that once an energetic electron crosses this line it is collected by the anode. This occurs because the potential drop in the anode plasma sheath is insufficient to reflect the high-energy electrons. As a consequence the high-energy, or primary, electrons are confined to the "primary electron region." The Maxwellian electron temperature also drops beyond the critical field line since the anode represents a sink for the electrons in the tail of the distribution. The low-energy electrons which exist outside the primary electron region are inefficient in ionizing neutrals, and consequently the plasma density in this region is much lower. Experimental results have shown that thruster performance is determined by the plasma conditions existing within the primary

electron region [18], and discharge chamber geometry changes external to this region have essentially no effect on thruster performance [6,19]. A comparison of the beam current density profiles of the axial and divergent field thrusters indicates a substantial improvement in the uniformity of the profile has been realized as a result of expanding the primary electron region to cover the entire chamber cross section at the downstream end of the thruster.

Another discharge chamber geometry which results in a further flattening of the ion beam profile is the radial field thruster illustrated in Figure 5c. This geometry has an extremely divergent, or radial, magnetic field arrangement. High-energy electrons emitted by the cathode are free to gyrate about field lines which are directed radially, and the electrons diffuse axially to the anode which is located in the upstream end of the chamber. Plasma property measurements in this thruster reveal a uniform density profile in the radial direction, and this uniformity is reflected in the beam profile shape illustrated in Figure 5c. The beam flatness parameter of this profile is about 0.51 and was the highest value reported in the literature at the time this investigation was initiated.

## Residence Time Theory

A comparison of the shape of the critical magnetic field line and the beam current density profile of the divergent field thruster illustrated in Figure 5b reveals a striking similarity. The beam current density profile is bell-shaped; much like the upstream boundary of the primary electron region. This observation suggests the ion

density near the screen grid is a function of the distance between the critical field line and the grids; a reasonable result considering the probability of a neutral encountering an ionizing electron as it drifts through a specified region.

If one considers neutral trajectories which are parallel to the thruster axis, the length of time a neutral atom resides in the primary electron region is given by the expression

$$\tau = \frac{L}{V_o} \tag{7}$$

where $\tau$ = neutral residence time

$L$ = distance between the critical field line and screen grid

$V_o$ = neutral particle speed

In order to encounter an ionizing collision the neutral atom must, on the average, reside in the primary electron region for a period equal to the characteristic time for ionization. The ionizing collision frequency for a neutral ground state atom interacting with primary and Maxwellian electrons is given by the expression

$$\nu = n_p \sigma V_p + n_m \langle \sigma V_m \rangle \tag{8}$$

where $\nu$ = ionizing collision frequency

$n_p$ = primary electron density

$n_m$ = Maxwellian electron density

$V_m$ = Maxwellian electron speed

$V_p$ = primary electron speed

$\sigma$ = ionization cross section

The symbol $\langle Q \rangle$ denotes the average of an energy-dependent quantity Q for the Maxwellian distribution function. Equating the neutral residence time with the reciprocal of the ionization frequency results in the following expression for the minimum depth of the primary electron region

$$L = \frac{V_o}{n_p \sigma V_p + n_m \langle \sigma V_m \rangle} \tag{9}$$

The neutral residence length L was calculated using Equation 9 and the measured plasma properties of a SERT II divergent field thruster. An iron filings map was used to determine the distance between the critical field line and the screen grid as a function of thruster radius. This distance was normalized by the calculated value of L for each radial position and in this form represents the probability for ionization. The results of these calculations are presented in Figure 6 along with the measured beam current density profile of this thruster. The similarity between these profiles suggests the neutral residence time consideration is a viable approach to shaping the beam current density profile. This implies the beam profile can be made more uniform by increasing the neutral residence time at the periphery of the discharge chamber. Since the residence time is determined by the distance between the critical field line and screen grid, moving the field line upstream at the thruster periphery should produce the

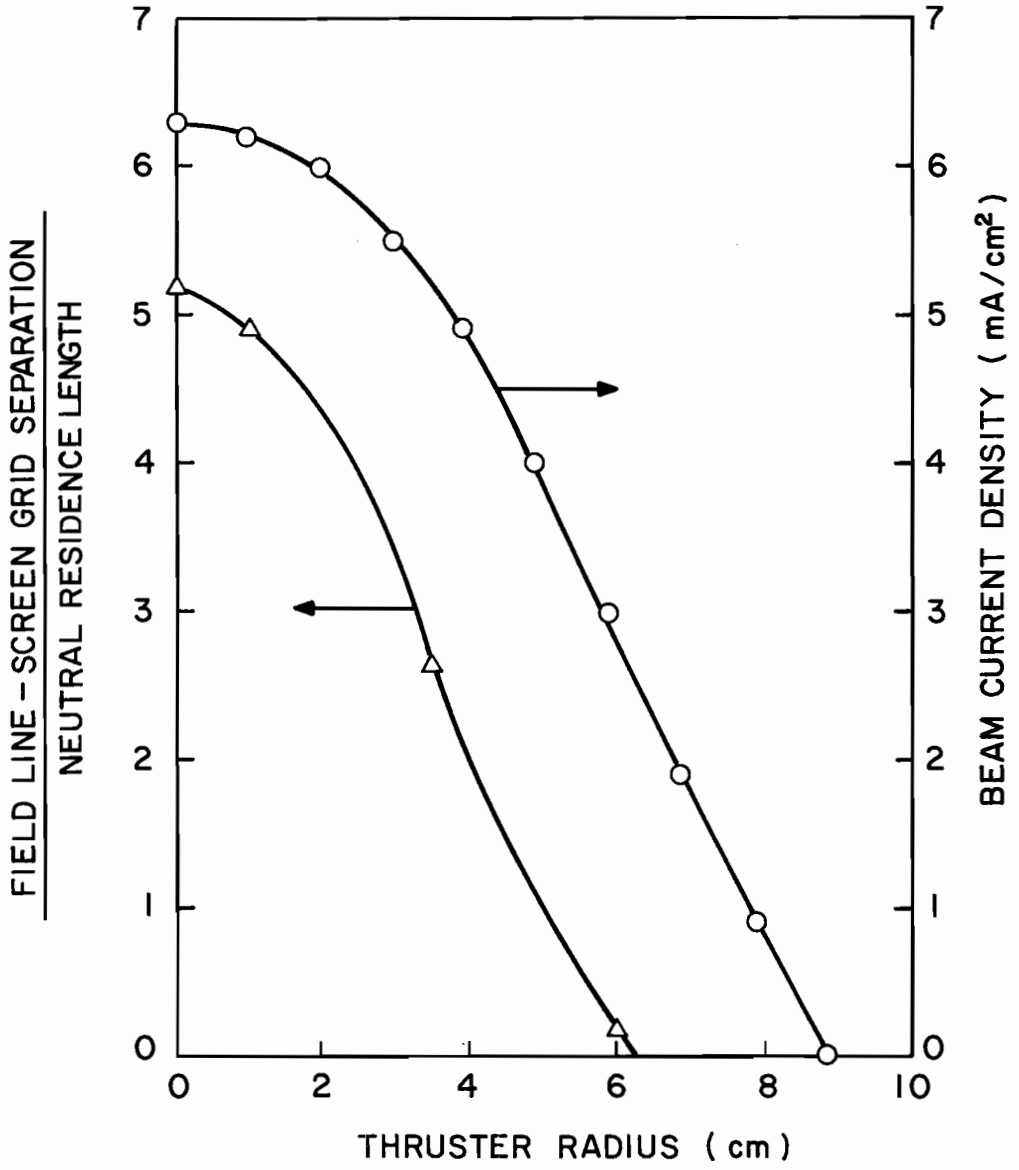


Figure 6. Variation of the ratio of field line-screen grid separation to neutral residence length and beam current density with thruster radius.

desired effect. However, this modification will increase the volume of the ion production region, and the effect of this increase on thruster performance must also be taken into account.

## Performance Considerations

The SERT II thruster is a high-performance engine which was developed during an extensive test program involving over 100 discharge chamber configurations [20]. The goal of the present investigation is to improve the beam profile flatness of this thruster as a means of extending the accelerator system lifetime. At the same time it is desirable to maintain, or perhaps improve upon, the high performance level of the SERT II thruster. For this reason, expressions relating the thruster power loss and propellant utilization to the discharge chamber geometry will be developed and used to predict thruster modifications which result in a uniform beam profile while maintaining good overall performance.

An expression for the propellant utilization efficiency can be derived by considering the single ion production and loss rates. It is assumed that uniform plasma properties exist within the ion production region, and that single ions are produced from the atomic ground state as a result of primary and Maxwellian electron impact. The ions are lost at the boundary of the production region at a rate given by the modified Bohm criterion [21]. Equating the production and loss rates for steady-state operation results in the following expression for the ion flux density

$$n_i V_i = n_o \nu V/A \tag{10}$$

where $n_i$ = ion density

$n_o$ = neutral density (ground energy state)

$V_i$ = modified Bohm velocity

$\nu$ = ionization collision frequency

$V/A$ = primary electron region volume-to-surface area ratio or characteristic length

The propellant utilization expression is obtained by multiplying the ion flux density by the screen grid effective open area* $A_i$ and dividing by the propellant flow rate $\dot{m}$

$$\eta_u = \frac{n_o \nu A_i V/A}{\dot{m}} \tag{11}$$

The neutral loss rate and propellant flow rate are related to the propellant utilization by the expression

$$\dot{n}_o = (1 - \eta_u)\dot{m} \tag{12}$$

where $\dot{n}_o$ is the neutral loss rate and is given by the free-molecular flow expression

---

*The effective open area of the screen grid is sometimes greater than the geometric open area due to the plasma sheath assuming a concave shape near the upstream side of the screen grid. The effect of this condition is to deflect ions into the beam which would otherwise have recombined on the screen grid.

$$\dot{n}_o = \frac{n_o V_o A_o}{4} \tag{13}$$

$A_o$ is the effective sharp-edged orifice area of the accelerator system. Combining Equations (11), (12), and (13) results in the desired expression for the propellant utilization

$$\eta_u = \frac{1}{1 + \frac{V_o A_o}{4\nu A_i V/A}} \tag{14}$$

In deriving Equation (14), it was assumed that single ions were produced from the atomic ground state. However, the excited states of mercury (particularly the $6^1P_1$ resonance state and $6^3P_2$ metastable state) contribute substantially to the total production rate [22]. To account for this, the ground state reaction rate $n_o\nu$ should be replaced by the total reaction rate which includes the excited states. In the final result, the collision frequency $\nu$ can be replaced by an effective collision frequency $\bar{\nu}$ which is given by the following expression

$$\bar{\nu} = \frac{\nu + \sum_i \frac{n_m^i}{n_o} \nu_m^i + \sum_i \frac{n_r^i}{n_o} \nu_r^i}{1 + \sum_i \frac{n_m^i}{n_o} + \sum_i \frac{n_r^i}{n_o}} \tag{15}$$

where the subscripts r and m refer to the resonance and metastable states, and the summation is over all excited states which contribute

significantly to the production of single ions. The collision frequencies $\nu_m^i$ and $\nu_r^i$ are given by Equation (8) with the cross section $\sigma$ replaced by the cross sections $\sigma_m^i$ and $\sigma_r^i$.

As a first approximation the discharge power, or beam ion production cost, can be expressed as the product of the plasma ion production cost $C_i$ and a factor which is the ratio of primary electron region surface area to screen grid effective open area [18]

$$P = C_i A/A_i \tag{16}$$

The plasma ion production cost represents the energy required to produce a plasma ion and consists primarily of inelastic collisional losses.

If one assumes the plasma properties remain constant, or vary in such a way that $C_i$ and $\bar{\nu}$ remain constant, then Equations (14) and (16) can be used to demonstrate the effect of discharge chamber geometry on thruster performance. For example, Equation (16) shows the discharge power will remain constant if the ratio $A/A_i$ is held fixed. This requirement and Equation (14) indicate the propellant utilization also remains constant if the ratio $A_o/V$ is fixed. These results are useful scaling relationships for the thruster designer. For instance, if the primary electron region has a cylindrical shape the performance parameters given by Equations (14) and (16) can be simplified to the following form by introducing the area and volume relationships for a cylinder of length $\ell$ and radius r

$$\frac{P}{C_i} = \frac{2}{\phi_i}\,(1 + \ell/r) \tag{17}$$

$$\eta_u = \frac{1}{1 + \dfrac{V_o\phi_o}{2\bar{\nu}\phi_i}\left(\dfrac{1}{\ell} + \dfrac{1}{r}\right)} \tag{18}$$

$\phi_o$ and $\phi_i$ are the effective open area fractions of the accelerator system to neutrals and ions, respectively. From these expressions one can see the importance of a large ion open area fraction in reducing discharge losses and increasing propellant utilization. The dependence of propellant utilization on the product $V_o\phi_o$ illustrates the importance of low chamber wall temperature, high molecular weight, and low neutral open-area fraction. Both the discharge power and propellant utilization depend on thruster radius in such a manner that large diameter thrusters should perform better than small diameter ones; a well-established experimental result. The length, on the other hand, is seen to have opposing effects on the performance parameters. This suggests small diameter thrusters can achieve acceptable propellant utilization efficiencies (at the cost of higher discharge losses) by increasing the chamber length. This prediction is also apparent if one considers the variation in the length-to-diameter ratios of optimum thruster designs [19].

The results of the preceeding analysis can be used for the somewhat different problem which is of interest to the present investigation. In this case the thruster radius is fixed, and the primary electron region can be modeled by a cylinder which lies along the axis of the

thruster as illustrated in Figure 7a. Due to the critical magnetic field line geometry, the effective radius of the cylinder is considerably smaller than the chamber radius. This confinement of the high-energy electrons to the center of the chamber results in a nonuniform beam current density profile as illustrated in the figure. In order to achieve a more uniform beam profile, the radius of the cylindrical primary electron region can be increased by means of a magnetic field modification. The basic difference between this problem and that of increasing the thruster diameter is that in the present case the same grids are used and thus the open area for neutral loss remains constant as the primary electron region is expanded radially outward. The effect this change will have on the thruster performance parameters can be predicted by use of the expressions derived previously.

Equations (14) and (16) were used to calculate thruster performance as a function of cylinder length for fixed values of cylinder radius. The quantity $V_o A_o / 4\bar{\nu}$ in Equation (14) was evaluated using the SERT II thruster geometry and propellant utilization. Calculations were made for cylinder radii of 4 cm and 6 cm which were chosen on the following basis. The SERT II thruster primary electron region has a volume-to-area ratio of 1.4 cm and the length at the thruster centerline is 9 cm. An equivalent cylinder having this same length and volume-to-area ratio has a radius of 4 cm. The 4 cm value also represents the radius at which the beam current density drops off rapidly as illustrated in Figure 6. The 6 cm value was chosen as representative of the radius to which the primary electron region can be expanded within a 15 cm diameter discharge chamber while maintaining adequate plasma confinement at the cylindrical chamber boundary. Different choices for the values

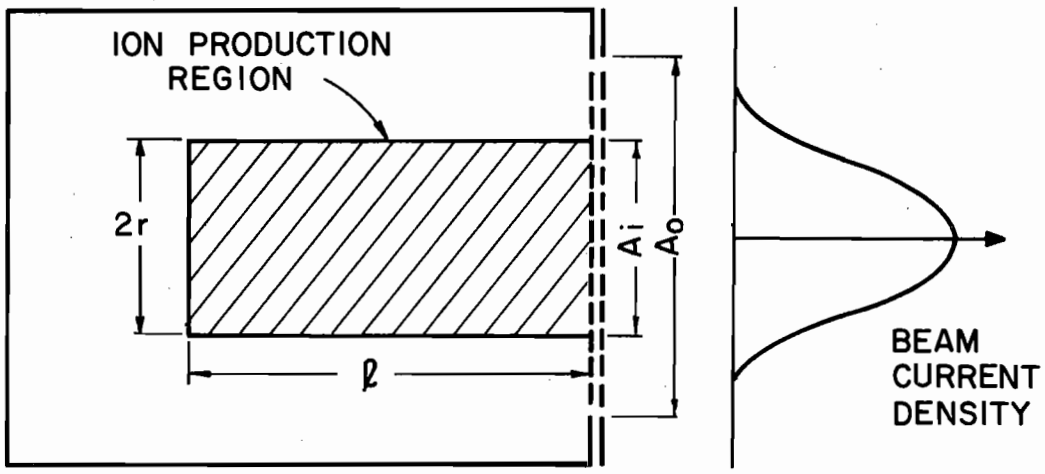


A. SERT II THRUSTER DISCHARGE CHAMBER MODEL AND ASSOCIATED BEAM PROFILE

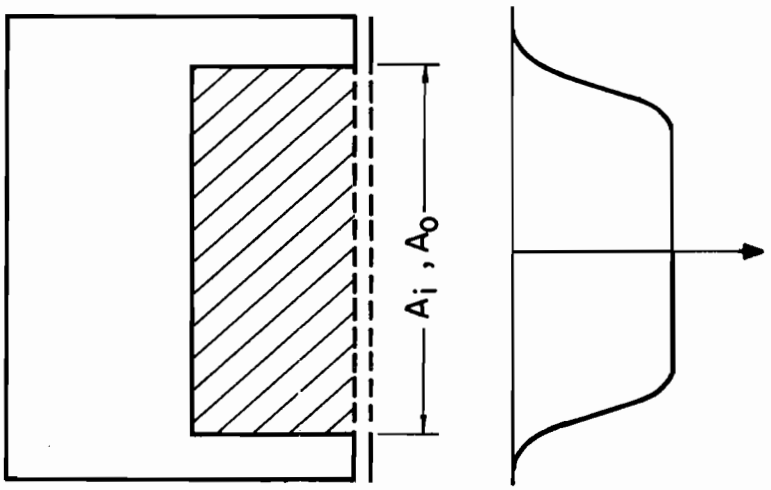


B. PROPOSED DISCHARGE CHAMBER MODIFICATION AND ANTICIPATED BEAM PROFILE

Figure 7. Discharge chamber models and their associated beam current density profiles.

of r would have no qualitative and little quantitative effect on the results of the calculations. The performance parameters calculated in the manner described above are presented in Figure 8. The numbers adjacent to the symbols on these curves indicate the primary electron region length in cm. It is interesting to note the similarity between these curves and performance plots obtained in an operating thruster (e.g., Figure 2). The increase in primary electron region length has the same effect as increasing the power input, while the increase in radius has the same effect as increasing the propellant flow rate. The data of Figure 8 indicate two important results: (1) increasing the diameter of the primary electron region produces substantial performance gains and (2) an optimum length exists for each radius which represents a compromise between discharge losses and propellant utilization. This latter result is analogous to the performance curve "knee" discussed earlier in the chapter.

The results of the analysis described in this and the previous section suggest the modification to the SERT II discharge chamber geometry illustrated in Figure 7b. The changes consist of (1) a magnetic field modification which increases the radius of the primary electron region and (2) a reduction in the primary electron region length. The anticipated results of these modifications are an improvement in both the uniformity of the ion beam current density profile and the thruster performance. The improvements predicted by the simple model are, of course, based on the assumption of constant plasma properties.

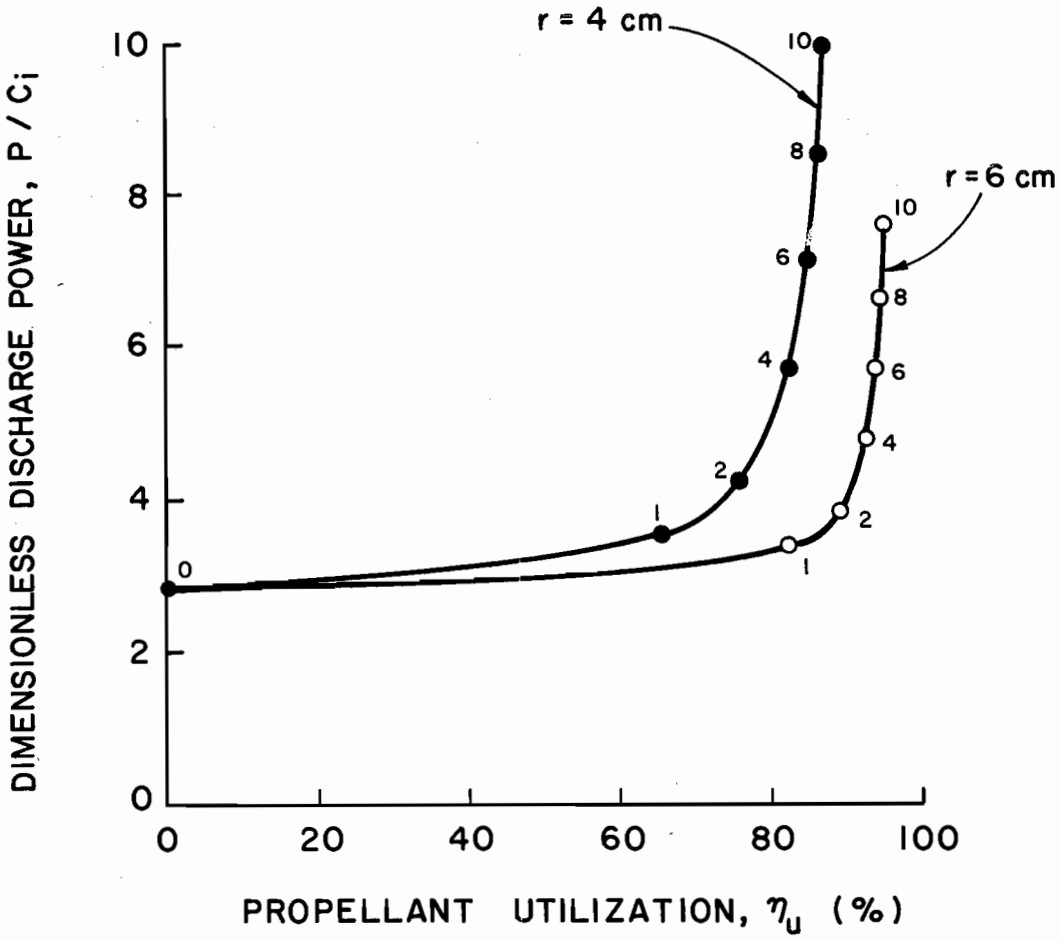


Figure 8. Calculated discharge chamber performance resulting from chamber length variations. Numbers adjacent to the symbols indicate the primary electron region length in cm.

## Double Ionization

The presence of doubly charged ions in the discharge chamber is undesirable for several reasons. Perhaps the most important of these is sputtering damage to the interior of the discharge chamber, particularly the baffle and screen grid. Therefore, the effect of the proposed discharge chamber modification on the double ion concentration should be assessed. Theoretical sutdies of the double ionization processes occurring in mercury electron-bombardment thrusters [22] have shown that the majority of the double ion production is due to electron bombardment of singly charged ions. This permits an approximate relationship for the double-to-single ion density ratio to be derived based on the assumption that double ions are produced solely from single ions. Equating the double ion production and loss rates results in the following expression for the double-to-single ion density ratio

$$\frac{n_{++}}{n_{+}} = \frac{\nu_{+}^{++}\ V/A}{\sqrt{2}\ V_i} \tag{19}$$

The collision frequency $\nu_{+}^{++}$ is given by Equation (8) with the cross section $\sigma$ replaced by the cross section for the production of double ions from single ions, $\sigma_{+}^{++}$. Comparing Equations (14) and (19) reveals the dilemma the ion chamber designer is faced with. In order to achieve high propellant utilization efficiencies the discharge chamber characteristic length V/A should be large, but according to Equation (19) this will result in a large double ion concentration.

Fortunately, the modification proposed in Figure 7b results in a predicted increase in the propellant utilization and a decrease in both the discharge power loss and double-to-single ion density ratio for the proper choices of the cylinder radius and length. This occurs since the open area to neutral propellant loss $A_0$ remains constant (the physical open area of the grids remains fixed), while the effective open area for ion extraction $A_i$ increases (ion production region expanded radially). In other words, the characteristic length V/A can be reduced, causing a reduction in the double-to-single ion density ratio. At the same time the quantity $A_iV/A$ can be increased, producing an increase in the propellant utilization; while $A/A_i$ can be reduced, producing a decrease in the discharge power loss. As an example, one might assume an initial primary electron region length and radius of 9 cm and 4 cm. If the primary electron region length were reduced to 4 cm and the radius increased to 6 cm, one could expect a 7 percent increase in propellant utilization, and a reduction in discharge power and double-to-single ion density ratio of 48 and 14 percent, respectively.

# III. APPARATUS

The discharge chamber used in this investigation is illustrated in Figure 9 along with the SERT II thruster discharge chamber. The major difference between the two configurations is the additional soft-iron pole piece located between the cathode and anode pole pieces. This modification produces the cusped magnetic field (CMF) geometry illustrated in the figure and results in an increase in the neutral residence length throughout most of the chamber. The SERT II thruster permanent magnets were replaced with electromagnets, and current to the magnet windings is provided by separate power supplies enabling independent control of the fields produced in the regions between the pole pieces. The original soft-iron thruster end plate was replaced with an aluminum plate, and the upstream electromagnets were designed to provide a permeable path between the cathode and center pole pieces. These features insure that the minimum path length through the plasma in the upstream end of the chamber is between the pole pieces and results in a predominantly radial magnetic field in this region.

The cusped magnetic field geometry is produced by maintaining the cathode and anode pole pieces at the same magnetic polarity. Reversing the current direction through either set of electromagnets changes the polarity of this set and results in a divergent magnetic field geometry. This unique feature allows radical changes in the magnetic field geometry to be made during thruster operation by simply reversing a

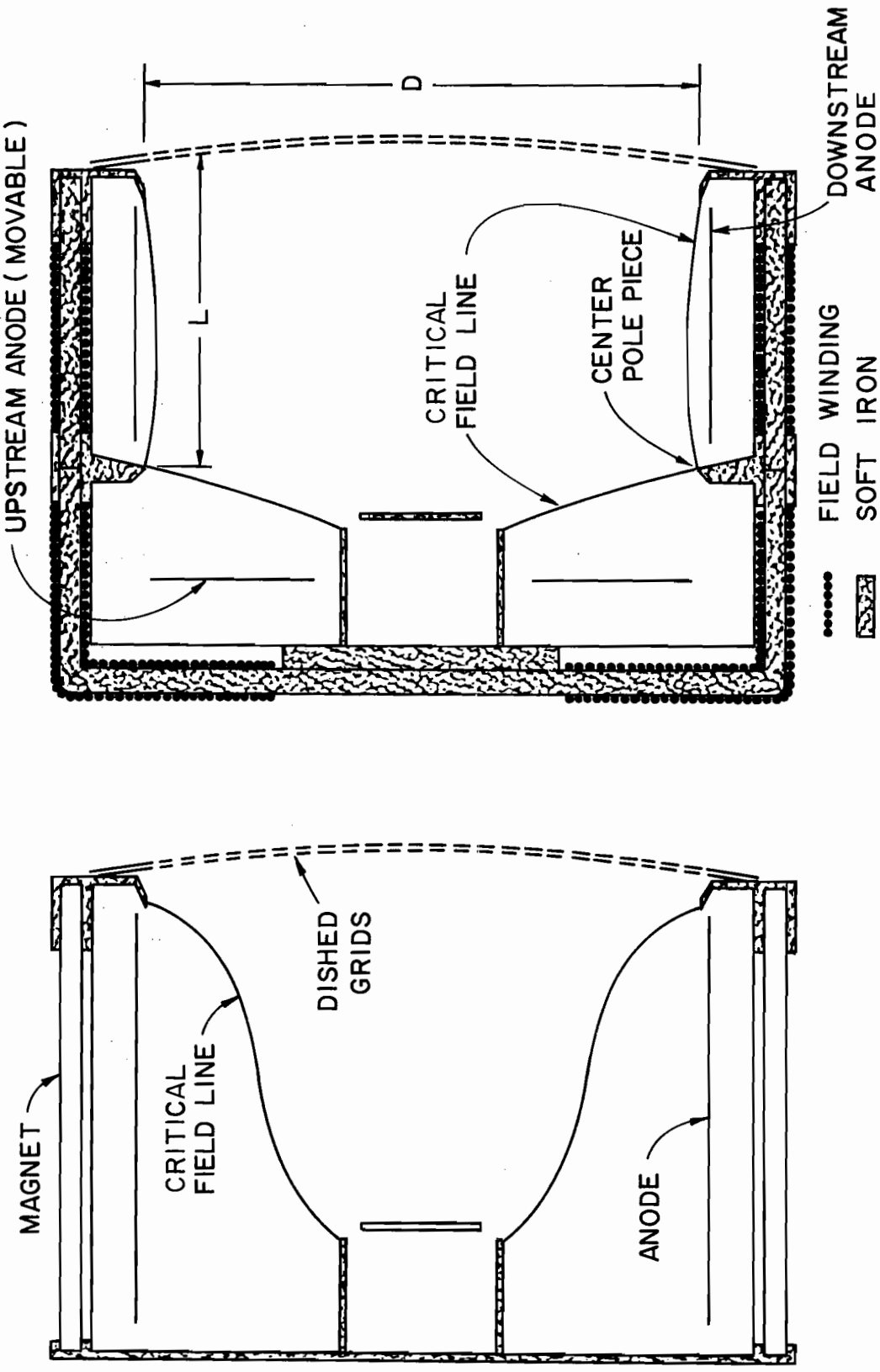


Figure 9. Comparison of the SERT II and cusped field thruster geometries.

switch. The purpose of the divergent magnetic field geometry was not to duplicate the SERT II magnetic field, but to allow the effects of two radically different magnetic field geometries to be evaluated with the same discharge chamber and identical operating conditions. An iron filings map illustrating the field geometries obtained with this arrangement is presented in Figure 10.

The length of the cylindrical anode located in the downstream end of the chamber was reduced to permit the installation of the center magnet pole piece, and a disc-shaped anode was installed in the upstream end of the chamber. This electrode is constructed of stainless steel screen which provides a uniform distribution of the neutral propellant flow to the discharge chamber. The axial position of the upstream anode can be varied during thruster operation, and this capability permits some operator control of the plasma properties and thruster performance by altering the plasma confinement at the upstream boundary of the primary electron region.

The separation distance L between the center and anode pole pieces determines the length-to-diameter ratio of the primary electron region, and this parameter is easily varied by replacing the downstream section of the chamber. The ability to vary the primary electron region length, magnetic field geometry, and anode position makes the discharge chamber designed for this investigation a unique and flexible research tool.

Some additional features include the following: (1) a variable magnetic baffle [23] which is useful in regulating the conductivity of the plasma in the annular region between the cathode pole piece and baffle, (2) individual vaporizers which permit independent control of the main and hollow cathode flow rates, and (3) large orifice diameter

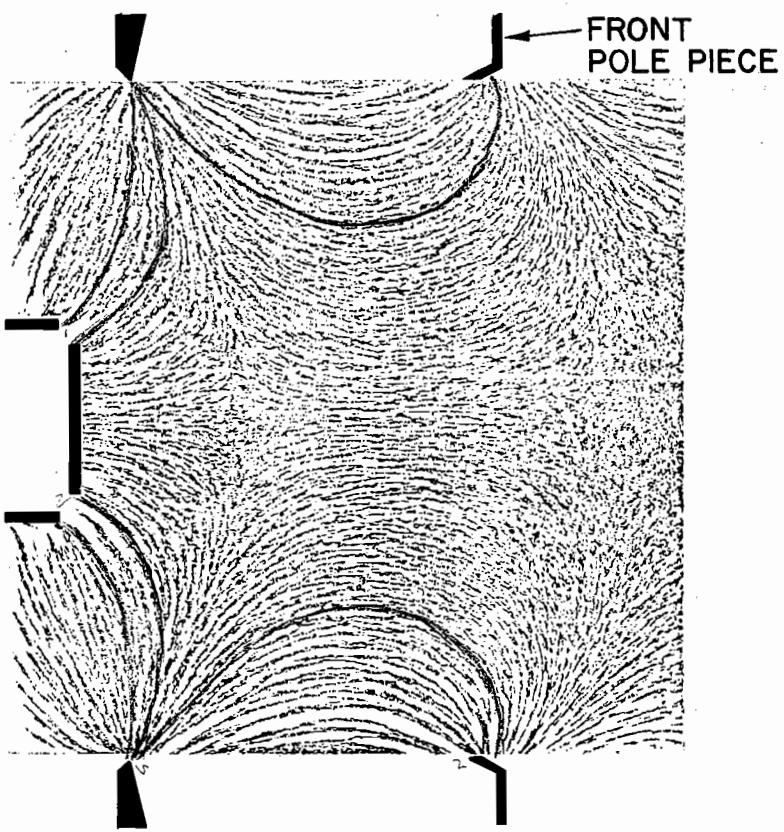


A. CUSPED FIELD GEOMETRY

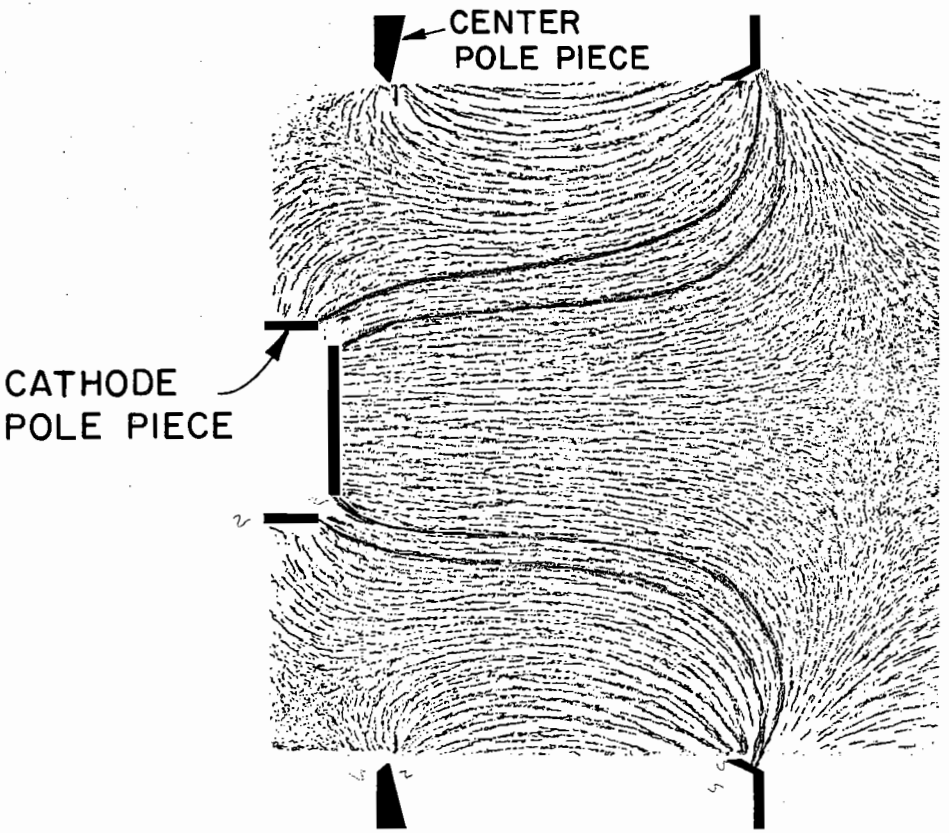


B. DIVERGENT FIELD GEOMETRY

Figure 10. Iron filings maps of the cusped and divergent magnetic field geometries (L/D = 0.53).

(0.5 mm) main and neutralizer cathodes which facilitate thruster operation at high beam current conditions.

The accelerator system is a high perveance dished type which provides good thermal stability and high beam current capacity at the specific impulse level desired for North-South stationkeeping of geosynchronous satellites. The screen electrode has a 76 percent open-area fraction to minimize ion recombination losses, and the accelerator electrode has a 54 percent open-area fraction to reduce neutral propellant loss. The accelerator grid is compensated to reduce the beam divergence and resultant thrust loss caused by the spherical shape of the accelerator system.

Mass flow rates are determined by timing the drop of the liquid mercury column in a precision bore glass tube, and these measurements are considered accurate to within ±3 percent. Currents and voltages used in performance calculations are measured using digital voltmeters, and all other electrical measurements are made with moving-coil meters. The accuracy of the digital meters is ±1 percent of full scale, while that of the panel meters is ±2 percent of full scale.

Plasma diagnostic information is obtained by the use of a movable Langmuir probe [24]. The collector is 0.074 cm diameter tantalum wire which extends 0.127 cm beyond an aluminum oxide insulator. A sliding protective sleeve is used to shield the probe and insulator from sputtered material when not in use.

A Faraday cup probe [24] is used to measure the ion beam current density profiles at a distance of 6 mm downstream of the accelerator grid. The double and single ion components of the current density profile are obtained by use of a collimating $\vec{E} \times \vec{B}$ momentum analyzer [25].

A precision stepper motor is used to pitch the analyzer to within $\pm 0.05^{o}$ of the desired angle, and an electrically driven worm drive assembly is employed to sweep the analyzer through the ion beam. The collector current is measured by a Model 416 Keithley picoammeter having an accuracy of ±3 percent of full scale.

The thruster was operated in the Ion Propulsion Research Facility at Colorado State University. The vacuum tank is a stainless steel cylinder 1.2 m in diameter and 4.6 m long and has a cryogenic target and liner. High-vacuum pumping is accomplished with an oil diffusion pump, and the tank liner, target, and diffusion pump baffles are cooled by circulating liquid nitrogen. During thruster operation the tank pressure is in the $10^{-6}$ torr range.

# IV. PROCEDURE

Thruster operating conditions were selected on the basis of using a 15 cm diameter mercury thruster to satisfy the North-South station-keeping requirements of a 700 kg geosynchronous satellite [26]. The specific impulse and thrust requirements of this mission dictate a 600 mA beam current with screen and accelerator grid potentials of +1000 V and -500 V, respectively [27]. Typical thruster operation at the performance curve knee results in a propellant utilization efficiency of about 80-85 percent. This range of utilization and the desired 600 mA beam current results in a nominal propellant flow rate of 730 mA which was the standard flow used in this investigation.

A 37 V anode potential was chosen as the nominal value and represents a compromise between ionization efficiency and thruster lifetime considerations. The anode power supply was operated in the current-limited mode, and the desired anode potential was achieved by varying the plasma conductivity in the baffle aperture region. The variation could be achieved either by altering the division between the cathode and main flow rates or by use of the variable magnetic baffle. In general it was found that a slight performance gain could be realized by using the cathode flow rate to achieve the desired voltage level, and the magnetic baffle was used primarily to stabilize thruster conditions immediately after startup. The anode potential could then be maintained by simultaneously reducing both the baffle magnet current

and cathode flow rate. The low cathode flow condition which was reached when the baffle circuit was de-energized is apparently responsible for the enhanced performance and has been observed by other investigators [20].

Four discharge chamber lengths were evaluated during this investigation and correspond to 100, 75, 63, and 38 percent of the SERT II thruster length. For all but the short discharge chamber, data were obtained for both the cusped and divergent magnetic field geometries with the upstream anode located in two different axial positions.

After the initial starting transient had decayed, the propellant flow rates were monitored and vaporizer currents varied until the desired flow rate was reached and three consecutive total flow readings were within ±1 percent of each other. As soon as the desired steady-state conditions were reached, data were recorded in the following sequence: (1) The Faraday cup probe was swept through the ion beam and the probe collection current recorded at $5^{o}$ intervals. These data were later punched on cards and used as input to a computer program which performed the integration for the beam current and beam flatness parameter. The integrated beam current determined in this manner was usually in agreement with the measured current to within ±2 percent. (2) The Langmuir probe was positioned at various radial and axial locations within the discharge chamber, and a continuous variation of collector current versus voltage was obtained by use of an x-y plotter. The spacing used in the probe surveys was 1.3 cm axially and 2.2 cm radially. This gave a total of 28, 20, 16, and 4 probe locations for the four chamber lengths investigated. The plotted Langmuir probe output was converted to digital form and punched on cards by use of an

Autotrol digitizer. These data were then used as input to a computer routine which performed calculations to yield the plasma properties. A numerical procedure for analyzing the Langmuir probe data was developed as a part of this investigation and is described by Beattie [28]. (3) The $\vec{E} \times \vec{B}$ momentum analyzer was swept through the ion beam at pitch angles of 0, 5, 10, and $15^{o}$. The collector current sensed by a picoammeter, as well as the output of a position-indicating potentiometer, was recorded by use of an x-y plotter. The current versus position curves were subsequently digitized and used as input to a computer routine which performs the double integration required to obtain the single and double ion beam current components. The integral equations used in the program are derived by Wilbur [22]. (4) Discharge power versus propellant utilization curves were obtained by varying the output current of the anode power supply. During the performance data acquisition the anode potential was allowed to vary in a manner determined by the conductivity of the discharge chamber plasma. Although this procedure permits rapid data acquisition and gives some idea of the performance trends, it should be pointed out that data obtained in this manner do not necessarily indicate the optimum thruster performance since they were obtained at a nonoptimum arc voltage level.

The use of a sliding protective sleeve on the Langmuir probe insulator was found to extend the useful lifetime of the probe by almost an order of magnitude. Unshielded probe insulators often became coated with sputtered conducting material resulting in an increase in probe collection area and erroneous plasma properties. The sleeve assembly effectively shielded the probe insulator from sputtered

material when the probe was not in use. By rotating the probe collector vertically upward the sleeve would slide downward and expose the collector to the plasma. After the probe survey was completed the probe was rotated downward and the sleeve would slide down the probe insulator and enclose the collector. The probe assembly was stored in a low-density region of the discharge chamber which further reduced the possibility of contamination and minimized any disturbing effects the probe might have on the plasma.

# V. EXPERIMENTAL RESULTS

The experimental results obtained with the cusped and divergent magnetic field geometries are presented in the first and second sections of this chapter. The third section presents the results for a radial magnetic field geometry which represents the limiting case of zero length-to-diameter ratio for the discharge chamber of both the cusped and divergent field geometries. The final section presents a comparison between the optimum cusped magnetic field discharge chamber and the SERT II thruster.

## Cusped Magnetic Field Thruster

Beam current density profiles are presented in Figure 11 for the three chamber length-to-diameter ratios investigated. Two profiles are presented for each chamber length; one corresponds to the upstream position* of the anode which resulted in optimum thruster performance, and the other corresponds to a downstream, or nonoptimum, anode position which degraded thruster performance. The beam flatness parameter was increased slightly with the anode in the nonoptimum position for all three discharge chamber lengths. However, changes in the flatness parameter were less than 3 percent suggesting the anode position has little effect on the beam flatness parameter. The effect of discharge

*The positions refer to the upstream anode. The downstream anode (e.g., Figure 9) was connected electrically in parallel with the upstream anode, and its position was fixed.

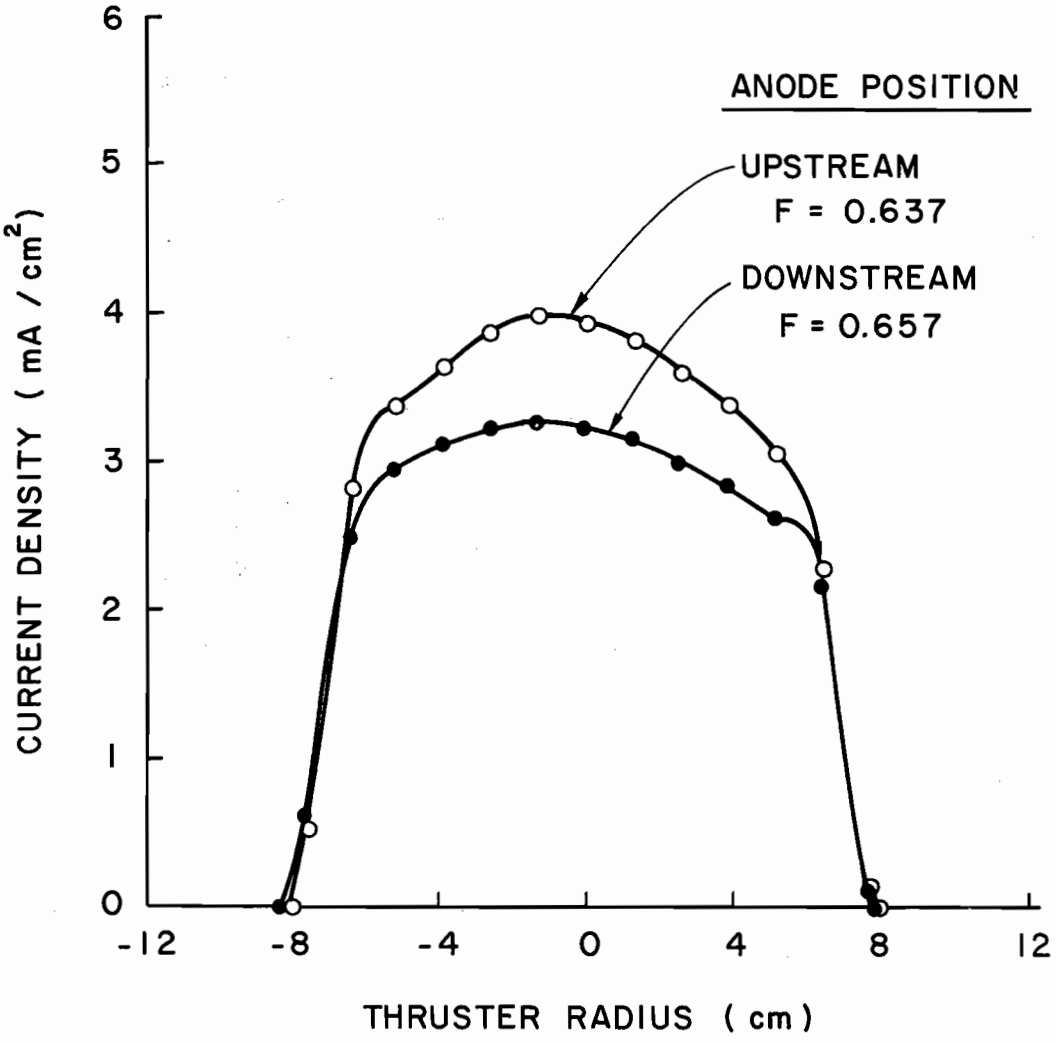


Figure 11a. Cusped magnetic field thruster beam current density profiles (L/D = 0.53). 730 mA propellant flow rate, 4 A anode current, 37 V anode potential.

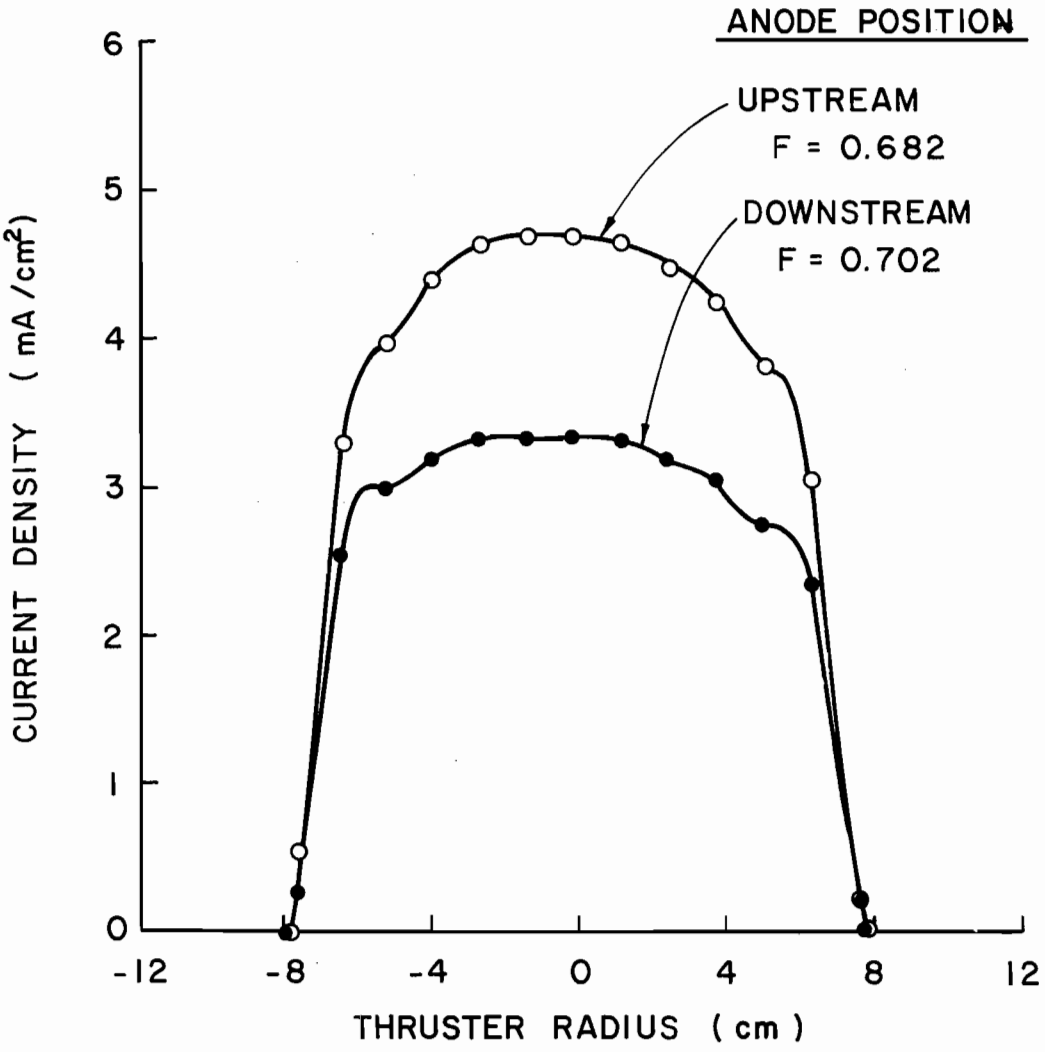


Figure 11b. Cusped magnetic field thruster beam current density profiles (L/D = 0.30). 730 mA propellant flow rate, 4 A anode current, 37 V anode potential.

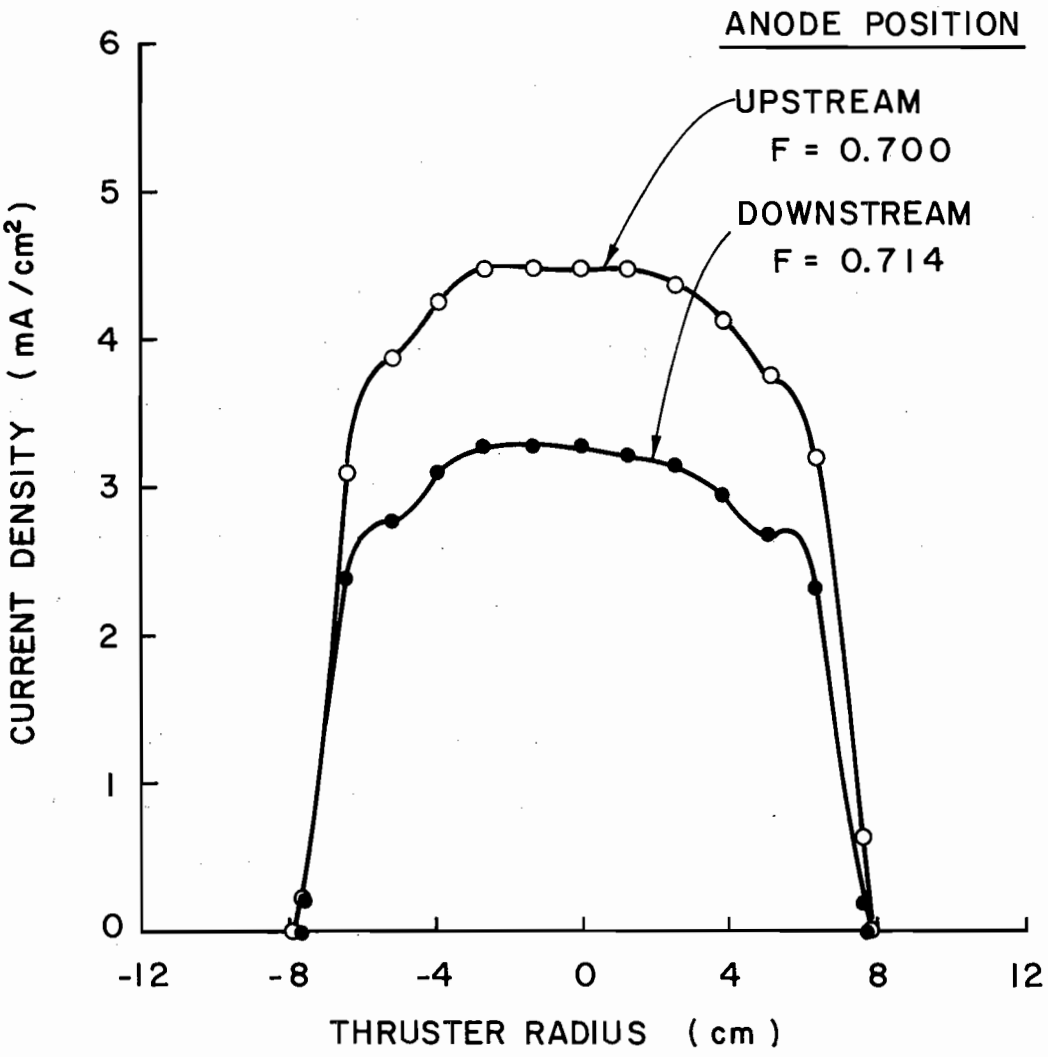


Figure 11c. Cusped magnetic field thruster beam current density profiles (L/D = 0.23). 730 mA propellant flow rate, 4 A anode current, 37 V anode potential.

chamber length reductions was to increase the beam flatness parameter some 12 percent as the chamber length was reduced to 63% of the SERT II thruster length. Figure 12 presents the beam current density profile for the short discharge chamber operated at a throttled propellant flow rate of 461 mA. Comparison of this figure with the corresponding profile of Figure 11c indicates a substantial increase in the beam flatness parameter was realized as a result of throttling the propellant flow rate.

Performance curves corresponding to the optimum upstream anode position are presented in Figure 13 for the three discharge chamber lengths investigated. The discharge power loss was reduced approximately 100 eV/ion as a result of decreasing the discharge chamber length-to-diameter ratio, and the short and intermediate chambers have about the same performance. The propellant utilization has not been corrected for the presence of multiply charged ions, and, as a result, utilizations of over 100 percent are indicated in Figure 13. The solid symbols on the performance curves indicate a 37 V anode potential and correspond to the operating conditions at which the Faraday, Langmuir, and $\vec{E} \times \vec{B}$ momentum analyzer probe data were recorded. The flagged symbols used in Figure 13 correspond to the nonoptimum anode position and indicate the severe performance degradation which accompanied the downstream movement of the anode. The close proximity of these data points indicates the performance is essentially independent of the discharge chamber length when the anode is in the downstream position.

The ratio of the double-to-single ion beam current components is presented as a function of discharge chamber length-to-diameter ratio in Figure 14. The downstream position of the anode is seen generally

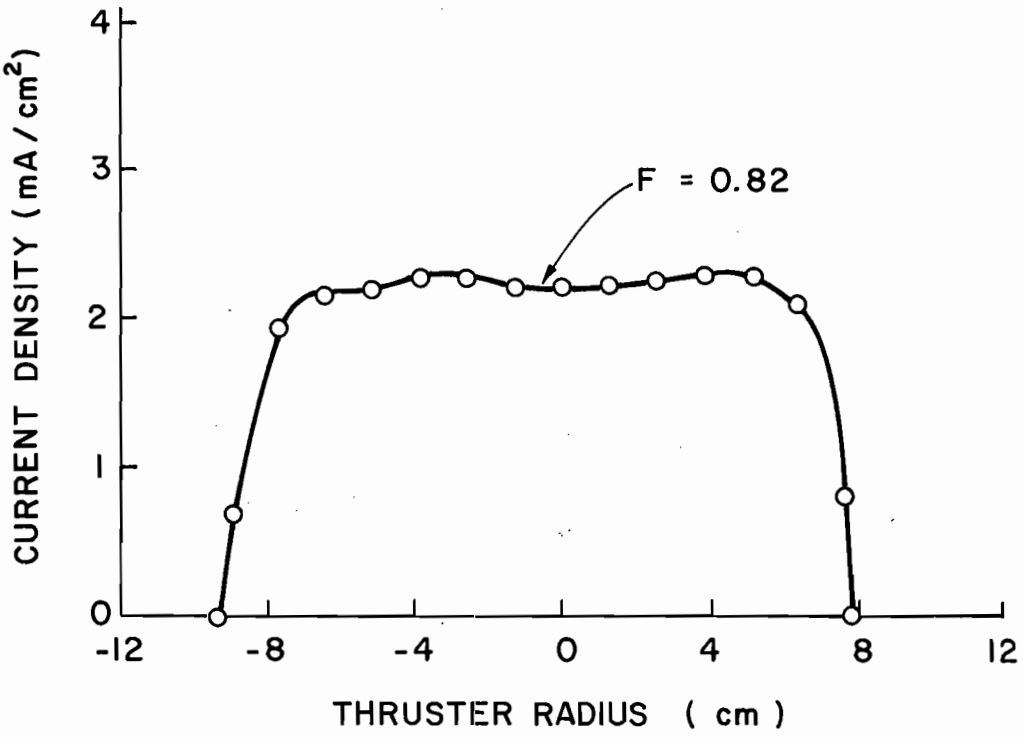


Figure 12. Cusped magnetic field thruster beam current density profile (throttled flow condition, L/D = 0.28). 461 mA propellant flow rate, 4 A anode current, 37 V anode potential.

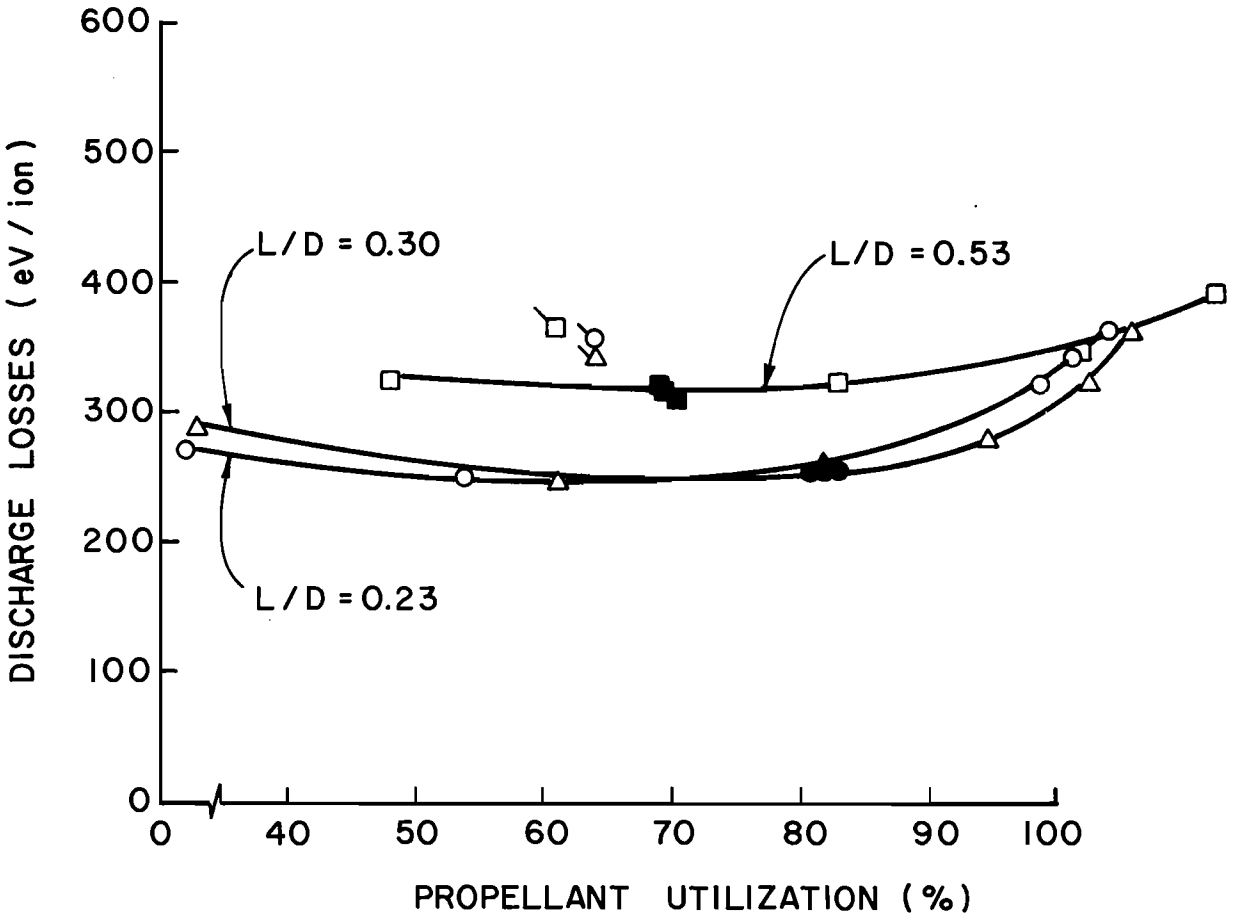


Figure 13. Cusped magnetic field thruster performance comparison. 730 mA propellant flow rate. Shaded symbols indicate the performance corresponding to 4 A anode current and 37 V anode potential.

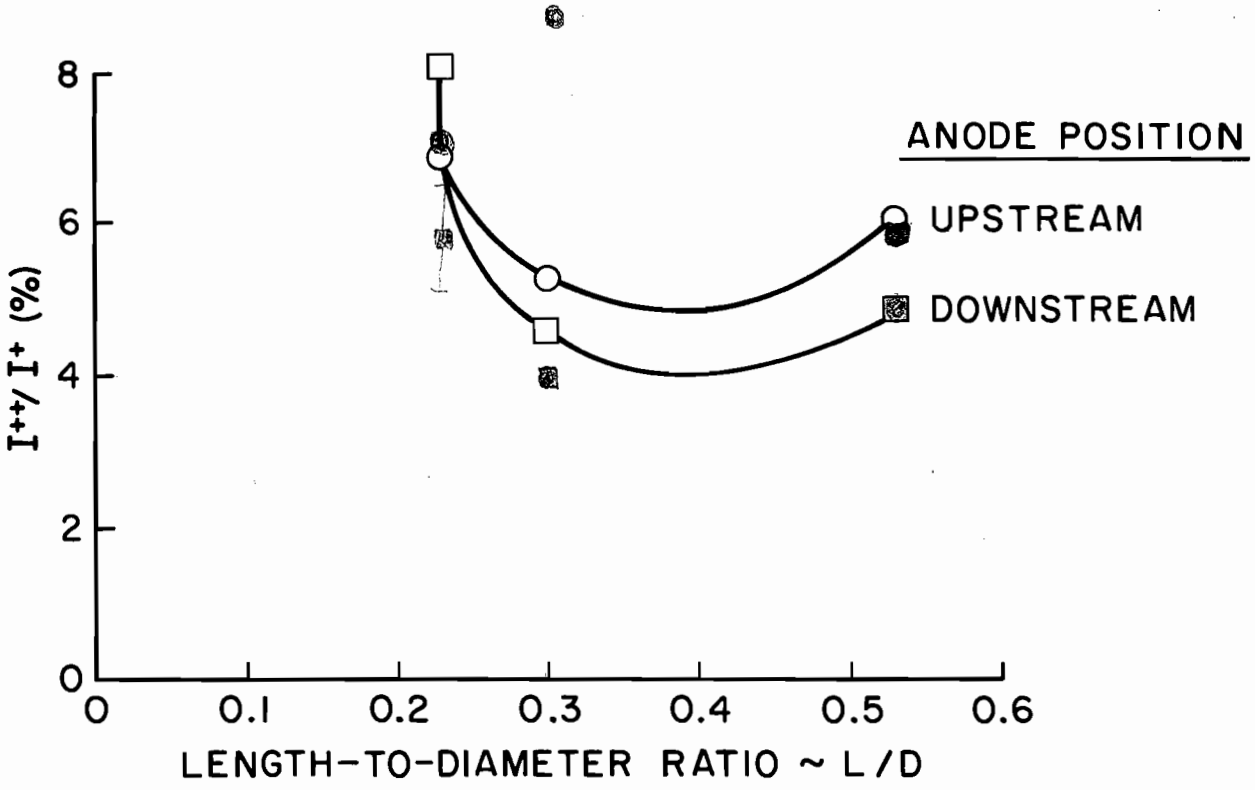


Figure 14. Cusped magnetic field thruster double-to-single ion beam current ratio. 730 mA propellant flow rate, 4 A anode current, 37 V anode potential.

to produce a slight reduction in the double-to-single ion current ratio. The intermediate chamber length resulted in the lowest double-to-single ion current ratio, and both the intermediate and long chambers are close to optimum from the standpoint of minimum double-to-single ion current ratio.

The results of Figure 14 indicate a relatively low double-to-single ion density ratio exists inside the various discharge chamber geometries. The double-to-single ion number density and current ratios are related by a factor of $2\sqrt{2}$. The factor 2 accounts for the higher charge and the factor $\sqrt{2}$ accounts for the higher velocity of the double ion. Thus the maximum current ratio of 8 percent is equivalent to a double-to-single ion density ratio near the screen grid of about 3 percent. The propellant utilization and thrust calculated from the measured beam current must be corrected to account for the error introduced by the presence of double ions in the beam current measurement. This may be done by use of the following relationships

$$\frac{(\eta_u)_{true}}{(\eta_u)_{calculated}} = \frac{1 + \frac{1}{2}\frac{I^{++}}{I^{+}}}{1 + \frac{I^{++}}{I^{+}}} \tag{20}$$

$$\frac{(T)_{true}}{(T)_{calculated}} = \frac{1 + \frac{\sqrt{2}}{2}\frac{I^{++}}{I^{+}}}{1 + \frac{I^{++}}{I^{+}}} \tag{21}$$

where $I^{++}/I^{+}$ is the double-to-single ion beam current ratio. These corrections are necessary since each double ion contribution to the measured beam current is $2\sqrt{2}$ greater than the single ion contribution due to the higher charge and velocity of the double ion. The propellant utilization and thrust correction factors calculated for a double-to-single ion current ratio of 5 percent, which is typical of Figure 14, are 0.976 and 0.986, respectively. These relatively small corrections correspond to a 37 V anode potential which is indicated by the use of shaded symbols in Figure 13. Propellant utilizations greater than the values indicated by the shaded symbols were obtained at higher discharge voltage levels which results in an increase in the production rate of doubly charged ions. As a result one would expect a larger correction to the measured propellant utilization at the higher power levels, and this is indicated in Figure 13 by the fact that the measured propellant utilization exceeds 100 percent. Attempts to obtain propellant utilization and thrust correction factors at high power conditions were unsuccessful due to the thermal expansion and subsequent shorting of the accelerator system caused by prolonged thruster operation at high discharge power levels. However, as mentioned earlier, the thruster would in general not be operated with an anode potential in excess of 37 V due to component lifetime considerations.

## Divergent Magnetic Field Thruster

Figure 15 presents beam current density profiles for the divergent magnetic field geometry. The optimum, or upstream, anode position generally resulted in a more uniform beam profile and the effect of the

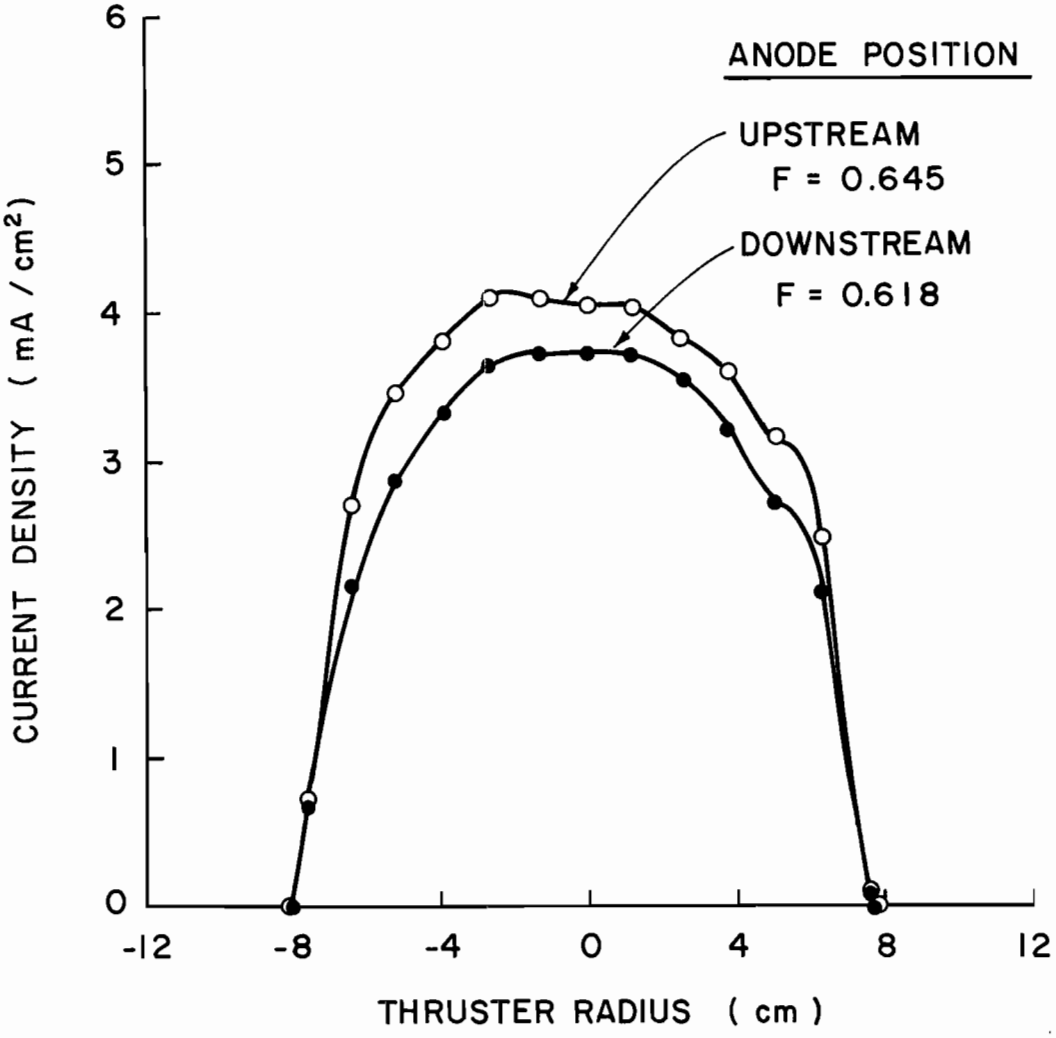


Figure 15a. Divergent magnetic field thruster beam current density profiles (L/D = 0.53). 730 mA propellant flow rate, 4 A anode current, 37 V anode potential.

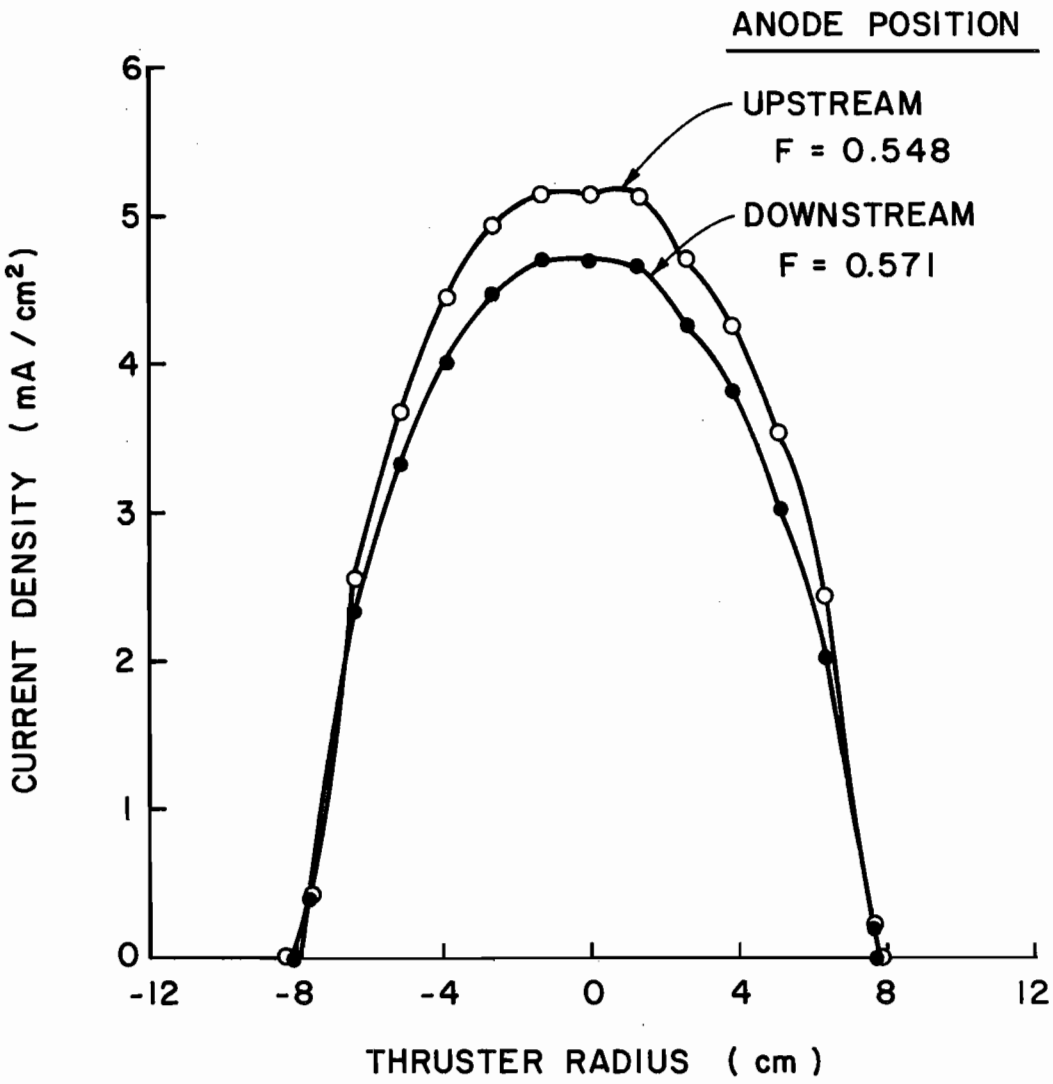


Figure 15b. Divergent magnetic field thruster beam current density profiles (L/D = 0.30). 730 mA propellant flow rate, 4 A anode current, 37 V anode potential.

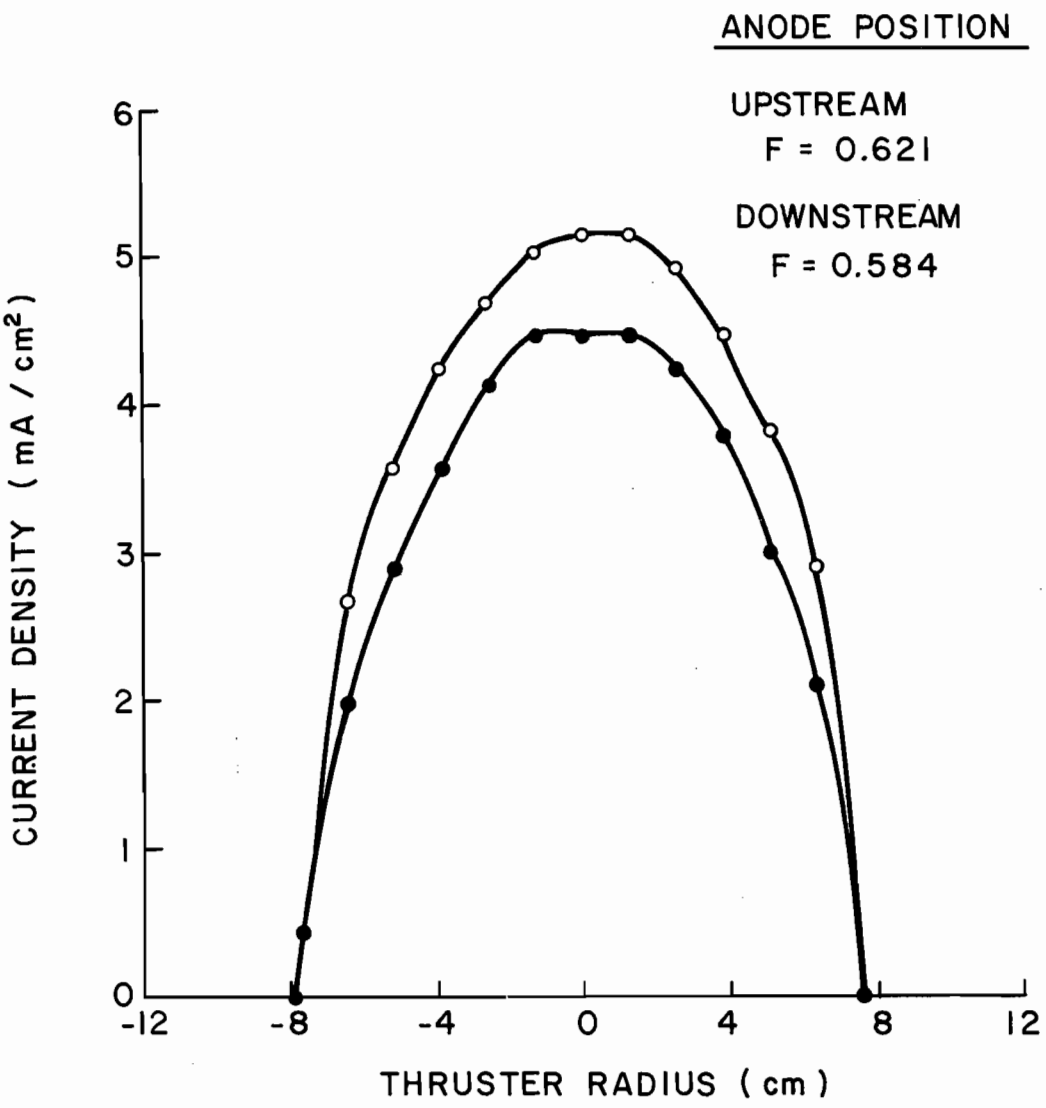


Figure 15c. Divergent magnetic field thruster beam current density profiles (L/D = 0.23). 730 mA propellant flow rate, 4 A anode current, 37 V anode potential.

nonoptimum, or downstream, location was relatively small. The beam flatness parameter decreased when the chamber length-to-diameter ratio was reduced from 0.53 to 0.3. Further length reduction produced an increase in beam profile flatness but not of the same magnitude as the original reduction. As a result the highest beam flatness parameter was realized with the longest discharge chamber; just the opposite of the results obtained with the cusped magnetic field geometry. With the exception of the intermediate discharge chamber length, the effect of moving the upstream anode to a nonoptimum position was to reduce the beam flatness parameter. However, as with the cusped field geometry, the effect of anode position was small enough that the flatness parameter can be considered essentially independent of anode position.

Performance data for the divergent magnetic field thruster are presented in Figure 16. The shaded symbols represent the 37 V anode potential and correspond to about the same power input to the discharge chamber. The effect of reducing the discharge chamber length was to increase the ion beam current which results in a reduction in the discharge power loss and an increase in propellant utilization. This effect was also realized with the cusped magnetic field geometry. The flagged symbols in Figure 16 indicate the performance level with the anode in the downstream position and demonstrate the substantial performance degradation which the nonoptimum anode location produced. A comparison of the effects of anode position on thruster performance for both the cusped and divergent field geometries shows the divergent field thruster was affected to a lesser degree than the cusped field thruster. The performance data of Figures 13 and 16 for the nonoptimum anode position suggest the chamber length variation had a greater effect on

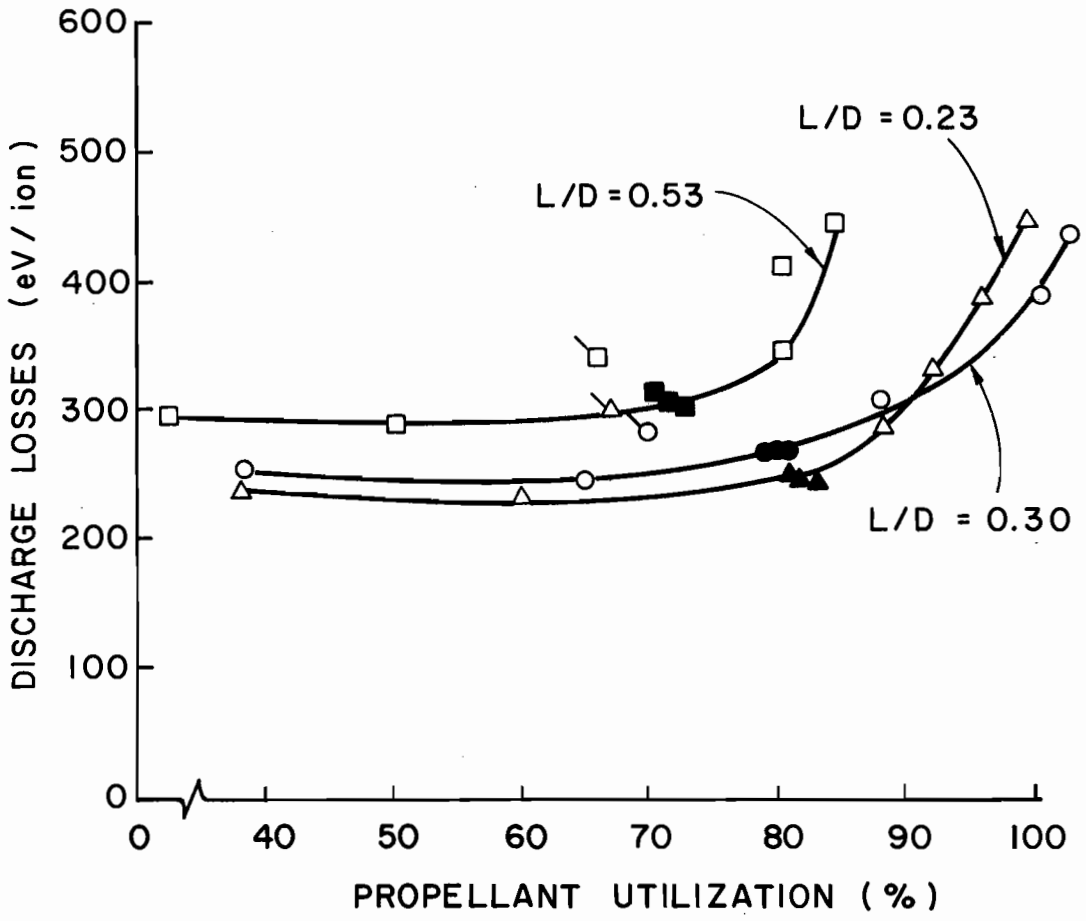


Figure 16. Divergent magnetic field thruster performance comparison. 730 mA propellant flow rate. Shaded symbols indicate the performance corresponding to 4 A anode current and 37 V anode potential.

the divergent field geometry than on the cusped field geometry. The performance data also indicate the baseline discharge power loss for a given chamber length is approximately the same for either magnetic field geometry. In addition, the performance curves for the divergent magnetic field geometry have a more pronounced "knee" than the corresponding data for the cusped magnetic field geometry.

The ratios of the double-to-single ion beam currents are presented in Figure 17 for the divergent magnetic field geometry. The effect of reducing the discharge chamber length is to increase the double-to-single ion current ratio, and the effect is more pronounced with the anode in the upstream position. The effect of the downstream anode position was to substantially lower the double-to-single ion current ratio. Comparison of Figures 14 and 17 indicates the cusped magnetic field discharge chamber geometry generally has a lower double-to-single ion density ratio with the anode in the upstream location. With the downstream anode position the divergent magnetic field geometry has a slightly lower double-to-single ion density ratio.

## Radial Magnetic Field Thruster

The limiting case of a zero length-to-diameter ratio discharge chamber was investigated for both the cusped and divergent magnetic field geometries by removing the downstream section of the discharge chamber. The resulting chamber geometry is illustrated in Figure 18. In this configuration the magnetic field is predominantly radial and the discharge chamber length is 38 percent of the SERT II thruster length. The end plate used in this thruster was identical to the SERT II design, and the dished grids were uncompensated and had a 58 percent

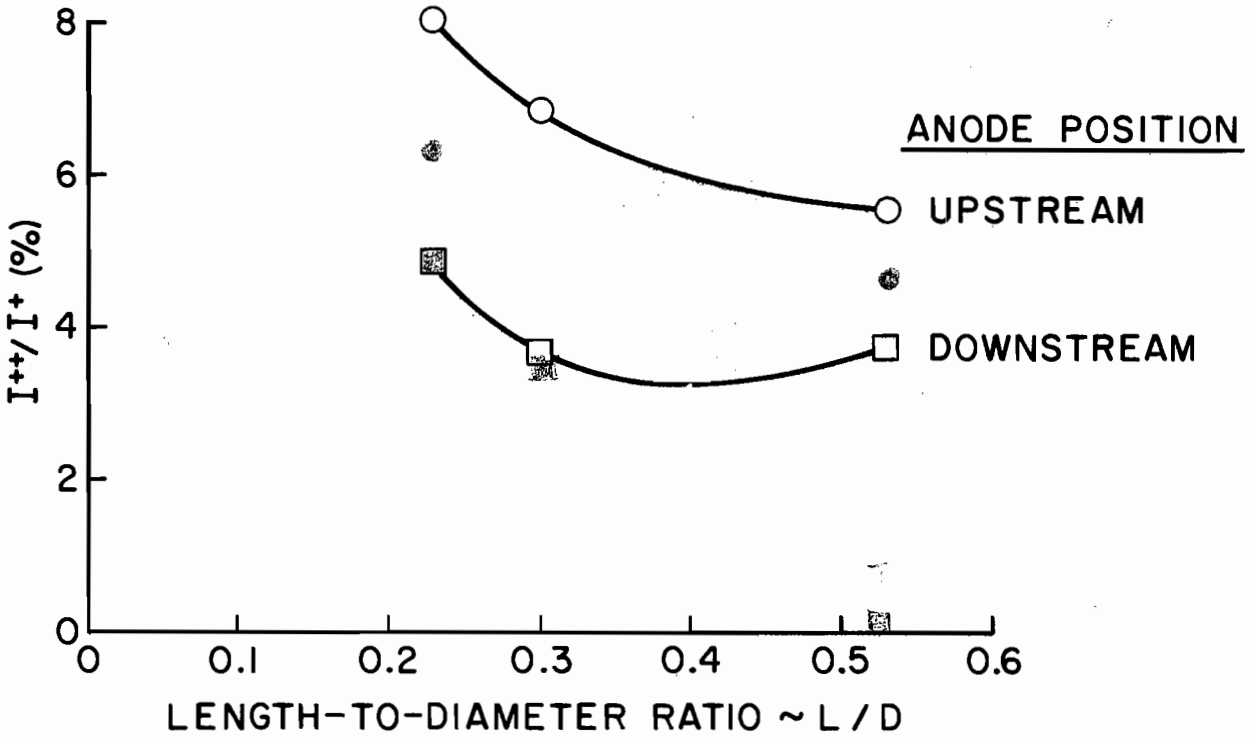


Figure 17. Divergent magnetic field thruster double-to-single ion beam current ratio. 730 mA propellant flow rate, 4 A anode current, 37 V anode potential.

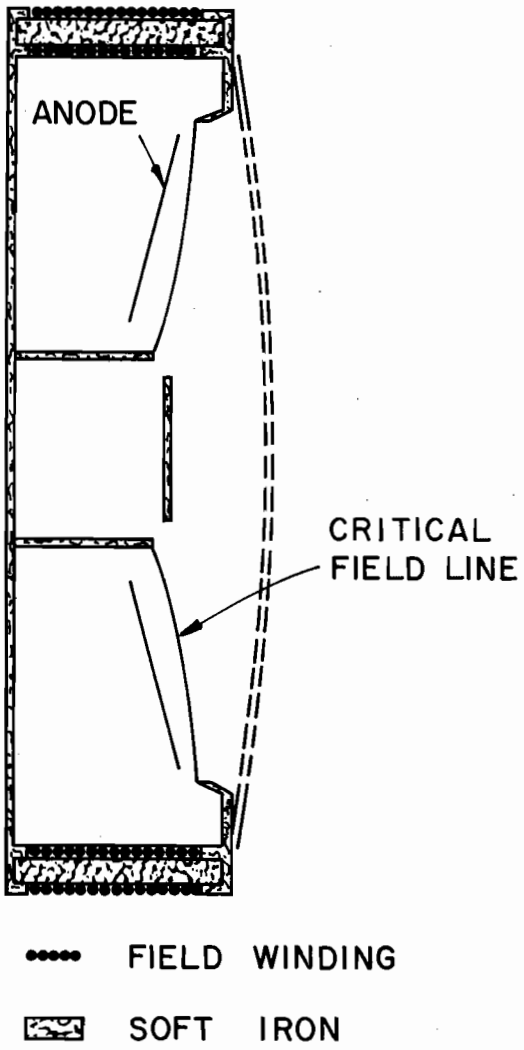


Figure 18. Radial magnetic field thruster geometry.

open-area fraction. These minor configuration changes are assumed to have little effect on the thruster beam profile and performance level,* and the results obtained with this thruster will be compared with the results presented in the preceeding sections.

The beam current density profile of the radial field discharge chamber geometry is presented in Figure 19. The profile is highly nonuniform (F = 0.23) and resembles the profile of the axial field thruster illustrated in Figure 5a. Performance data for the radial field thruster geometry are presented in Figure 20 and indicate a serious performance degradation resulted from reducing the chamber length-to-diameter ratio to zero. Although the baseline discharge loss is comparable to the cusped and divergent magnetic field thrusters, the propellant utilization at the knee of the performance curve is only about 40 percent.

### Comparison With The SERT II Thruster

Nondimensional ion beam current density profiles are presented in Figure 21 for the SERT II and cusped magnetic field thrusters. The integrated beam current is the same for each profile, and when normalized in this manner the reciprocal of the peak normalized current density is numerically equal to the beam flatness parameter. The ideal current density profile has a normalized current density of unity and is shown in Figure 21 for comparison. The normalized profiles indicate a dramatic improvement over the SERT II thruster beam profile uniformity

*The cusped magnetic field thruster was operated with these same minor changes, and the effects on beam profile flatness and performance level were quite small.

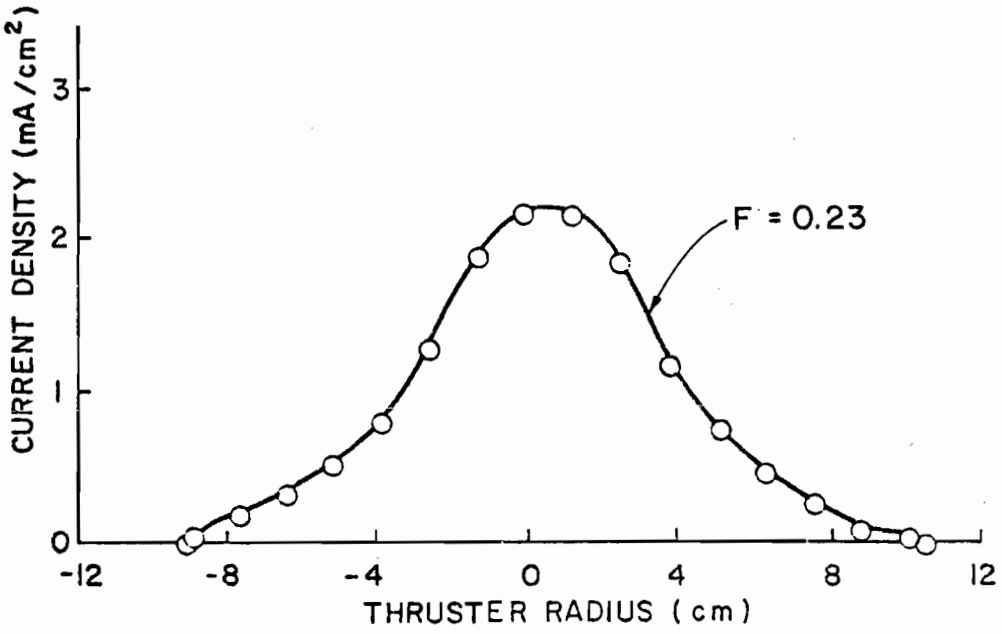


Figure 19. Radial magnetic field thruster beam current density profile. 492 mA propellant flow rate, 3.3 A anode current, 37 V anode potential.

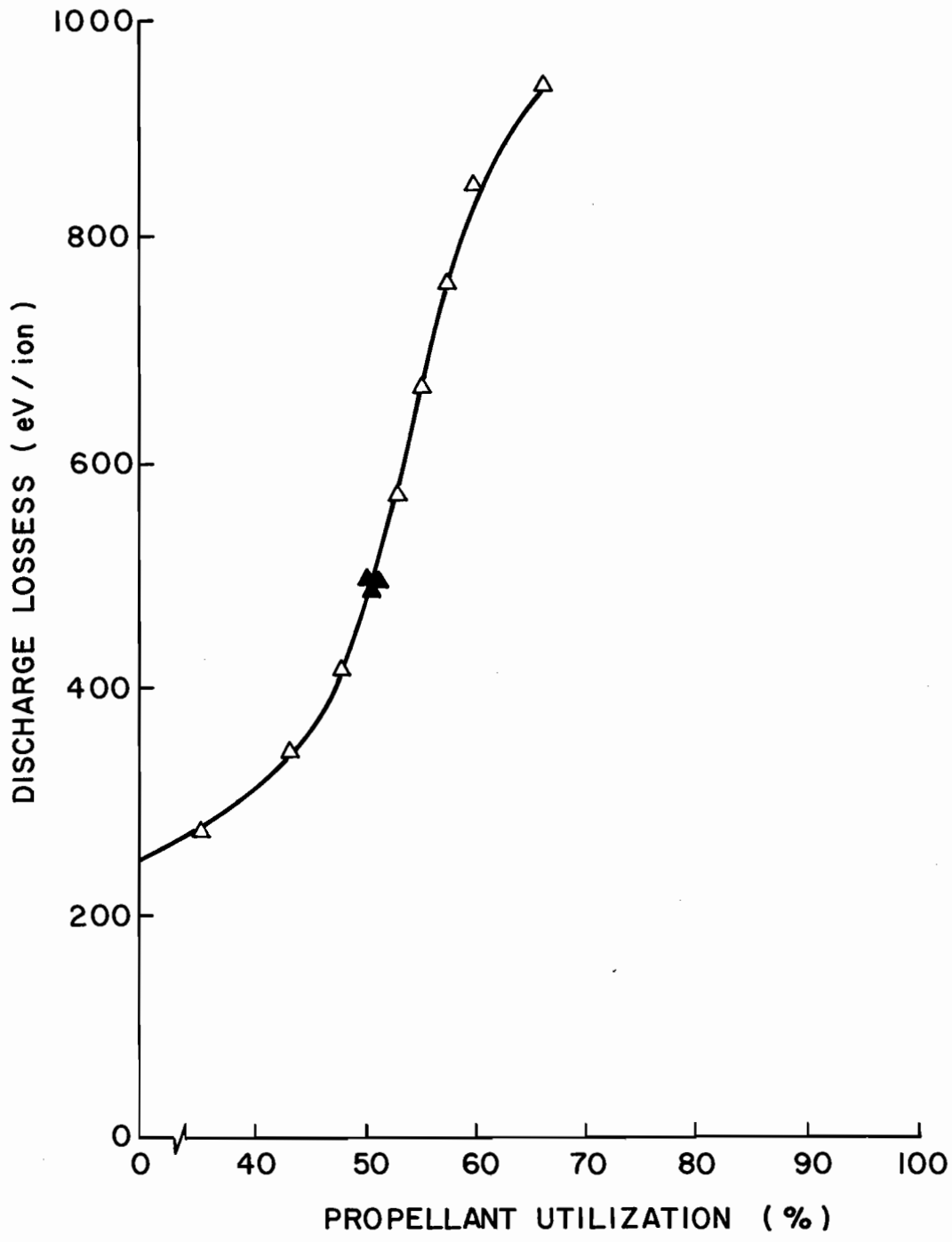


Figure 20. Radial magnetic field thruster performance.
744 mA propellant flow rate.

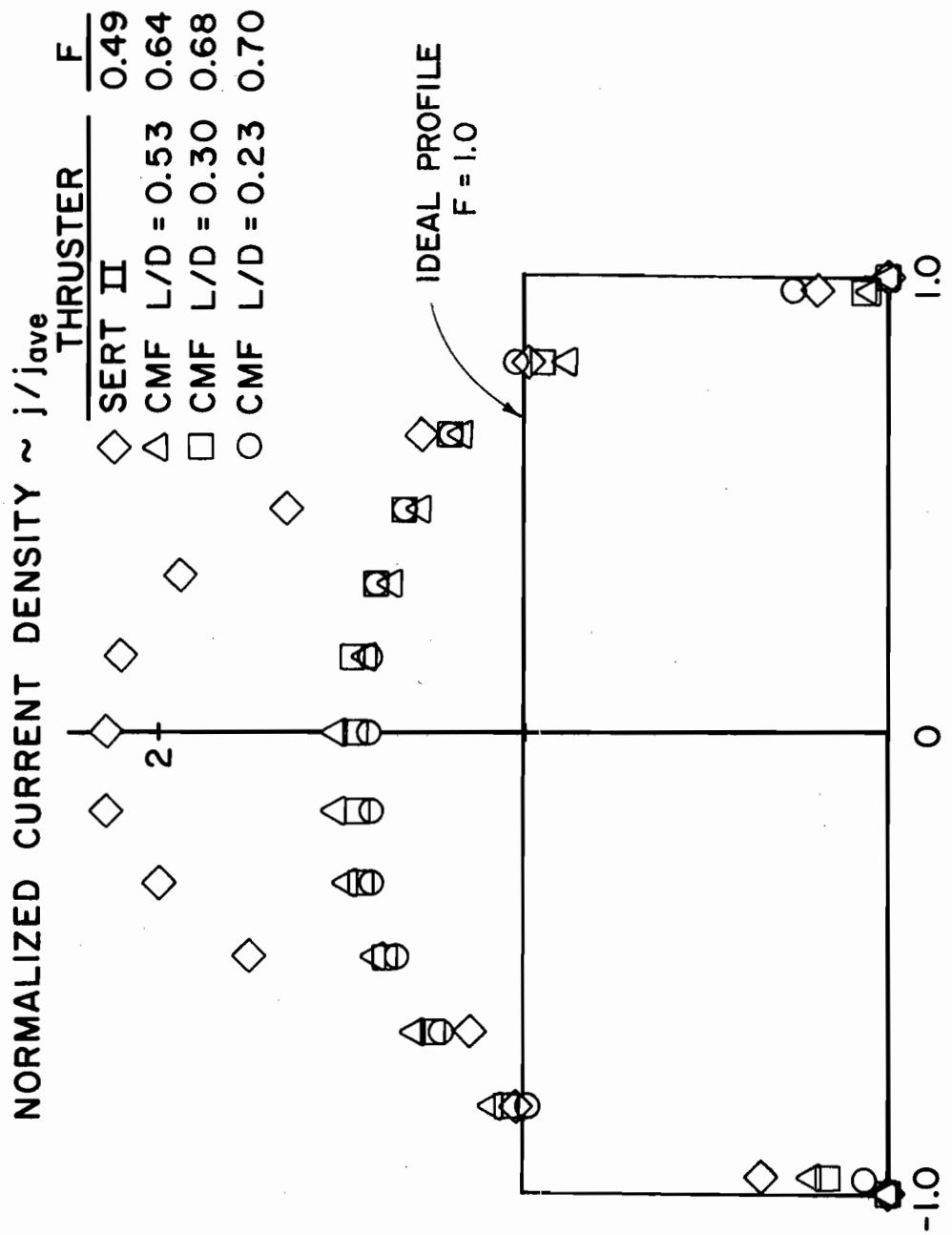


Figure 21. Comparison of the SERT II and cusped magnetic field thruster beam current density profiles. 730 mA propellant flow rate, 4 A anode current, 37 V anode potential.

was accomplished with the cusped magnetic field discharge chamber design. The beam flatness parameter of the cusped field geometry is about 30 percent greater than the SERT II thruster value for the same discharge chamber length. The flatness parameter of the shorter chamber geometries is about 40 percent higher than the SERT II thruster value.

A performance comparison between the SERT II and the cusped field thrusters is presented in Figure 22. The cusped field data correspond to a discharge chamber length-to-diameter ratio of 0.3 and indicate a slightly higher baseline discharge loss than the SERT II thruster. The performance at the "knee" of the curves is nearly identical for both thrusters.

A summary of the thruster operating conditions, performance level, beam flatness, and double-to-single ion current ratio is presented in Table 1 for the SERT II and optimum cusped field thrusters. These data indicate the cusped magnetic field thruster offers substantial improvements in the uniformity of the beam and double ion current density profiles. The increase in the flatness parameters of these profiles is about 40 percent. In addition, the double-to-single ion current ratio in the cusped field geometry is approximately 36 percent less than the corresponding SERT II thruster value. The performance degradation accompanying these improvements is relatively small; approximately 7 percent increase in discharge power loss and a 4 percent reduction in propellant utilization.

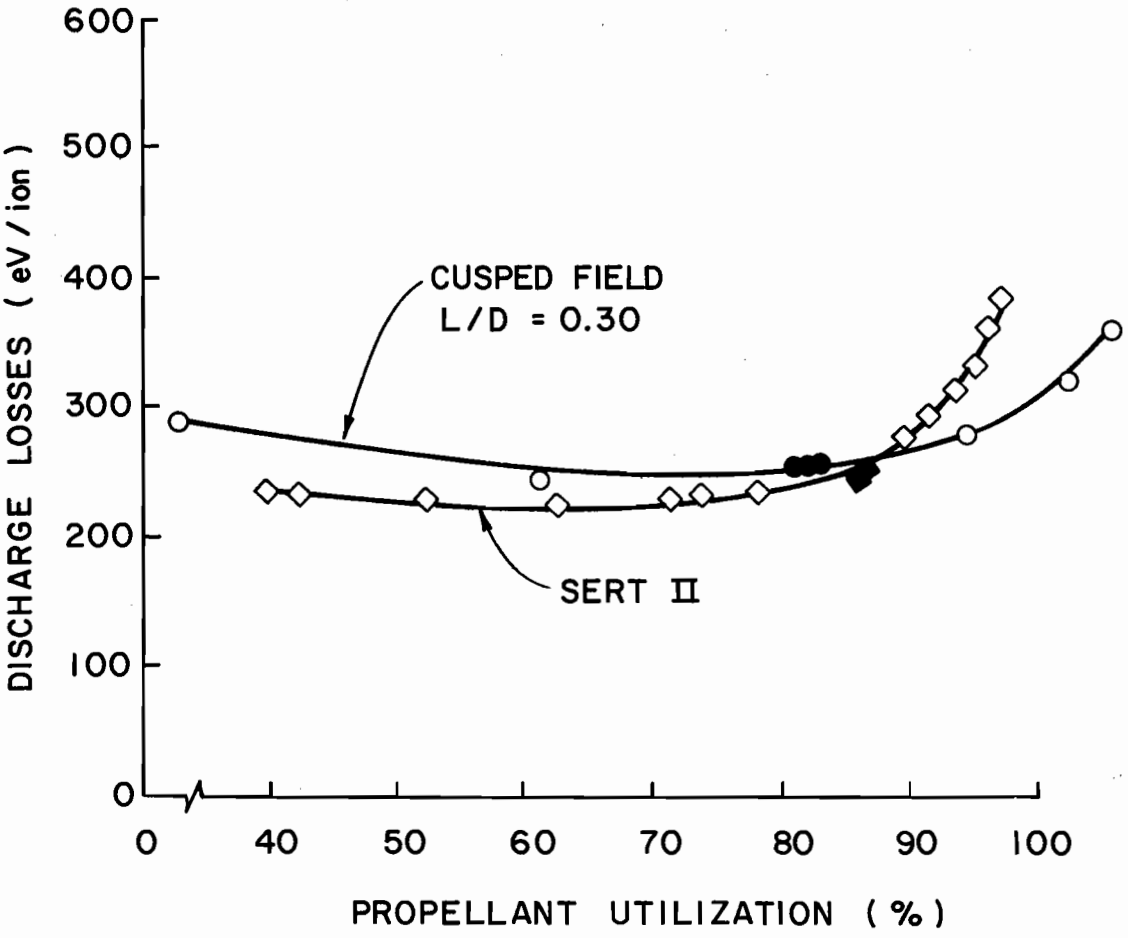


Figure 22. Comparison of the SERT II and cusped field thruster performance. 730 mA propellant flow rate.

TABLE 1

COMPARISON OF THE SERT II THRUSTER AND OPTIMUM CUSPED FIELD THRUSTER OPERATING CONDITIONS AND PERFORMANCE PARAMETERS

| | SERT II THRUSTER | CUSPED FIELD THRUSTER (L/D=0.3) |
|---|---|---|
| Operating Conditions | | |
| Anode Potential (V) | 38 | 36.7 |
| Anode Current (A) | 4.1 | 4.3 |
| Beam Current (mA) | 654 | 625 |
| Propellant Flow Rate (mA) | 725 | 730 |
| Performance Parameters | | |
| Discharge Power Loss (eV/ion) | 239 | 256 |
| Corrected Propellant Utilization (%) | 86.8 | 83.5 |
| Double-to-Single Ion Current Ratio (%) | 8.1 | 5.2 |
| Beam Flatness Parameter | 0.49 | 0.68 |
| Double-Ion Beam Flatness Parameter | 0.27 | 0.38 |

# VI. DISCUSSION OF THE EXPERIMENTAL RESULTS

A discussion of the improvement in the ion beam uniformity which resulted from the cusped magnetic field modification is presented in the first section of this chapter. The next section describes a procedure which was developed for use in defining the ion production region of an arbitrary discharge chamber configuration. The following section presents the volume-averaged plasma properties for the ion production region defined in this manner. These properties are then used to explain many of the performance characteristics presented in Chapter V. A comparison between the experimental results and the predictions based on the performance and double ionization considerations of Chapter II is presented in the next part of the chapter. The final section discusses the beam profile shape and performance characteristics of the radial field thruster configuration.

## Beam Profile

The cusped magnetic field discharge chamber modification was quite successful in improving the uniformity of the SERT II thruster beam current density profile. For the same discharge chamber length, the cusped magnetic field configuration resulted in an increase in the SERT II thruster beam flatness parameter of about 30 percent (from 0.49 to 0.64). Reducing the discharge chamber length resulted in further improvements in the beam profile uniformity, and with the chamber length

reduced to 63 percent of the SERT II thruster value the flatness parameter was about 40 percent higher. The improvement in the ion beam flatness is due to the existence of a radially uniform ion density profile near the screen grid. This is illustrated in Figure 23 which shows the ion density profiles for the three different discharge chamber lengths. The improvement in the ion beam current density uniformity which accompanied the discharge chamber length reductions can be explained by considering the magnetic field variations produced by these reductions. Figure 24 shows the radial variation in the axial component of the magnetic field at a point midway between the center and anode pole pieces. These measurements indicate a substantial reduction in the magnetic field fringing was realized with the shorter discharge chambers, and this produces a relatively field-free region over a large fraction of the discharge chamber volume. The absence of a significant magnetic field eliminates the need for a radial plasma density gradient and results in much more uniform ion density and beam current density profiles.

## Ion Production Region

In divergent field thrusters the region of the chamber where the bulk of the ion production occurs has been defined by considering an iron filings map of the magnetic field configuration. Using this procedure the upstream boundary of the ion production region can be approximated by the "critical" magnetic field line which is defined as the innermost field line which intercepts the cylindrical anode. In the cusped field thruster discharge chamber the definition of the critical field line is complicated by the presence of the additional

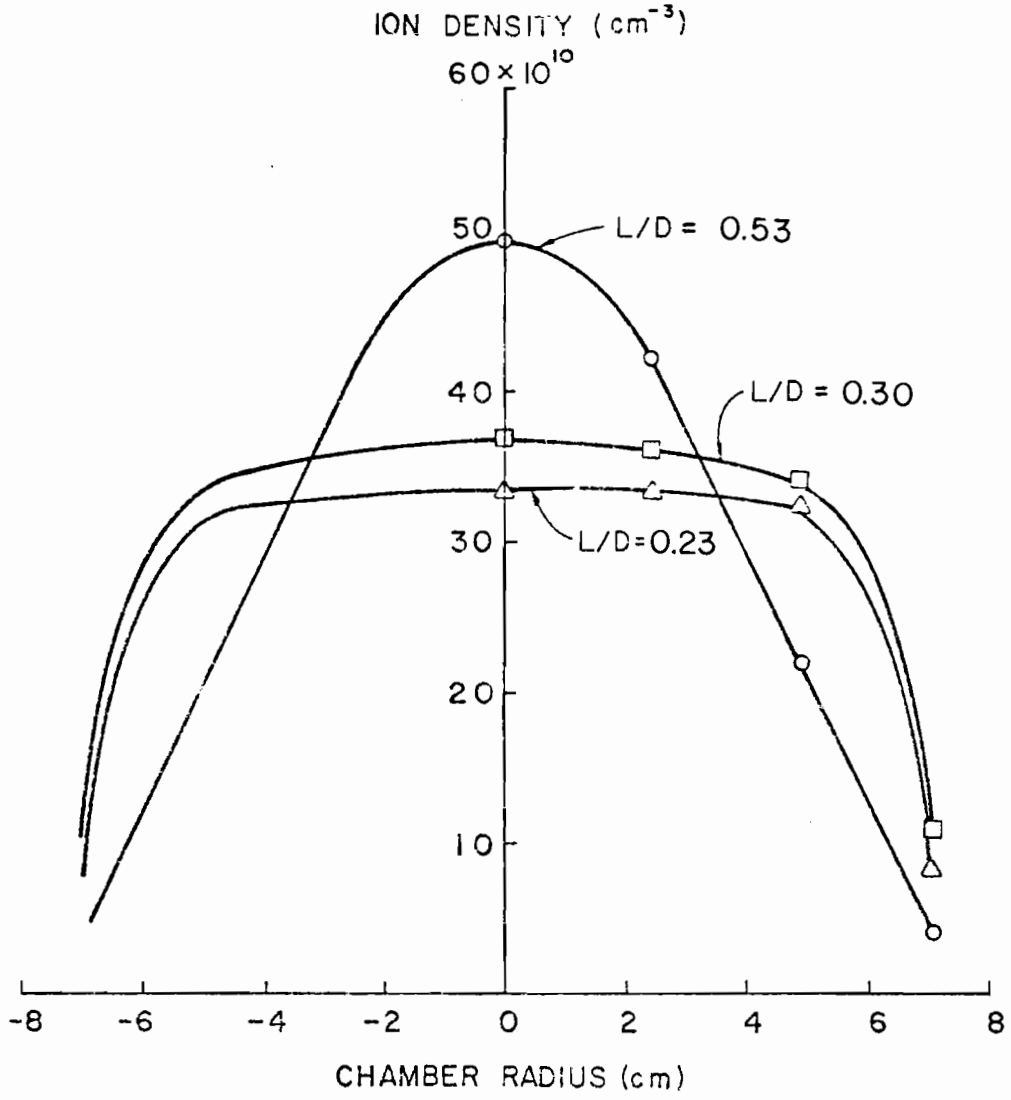


Figure 23. Cusped magnetic field thruster ion density profiles.

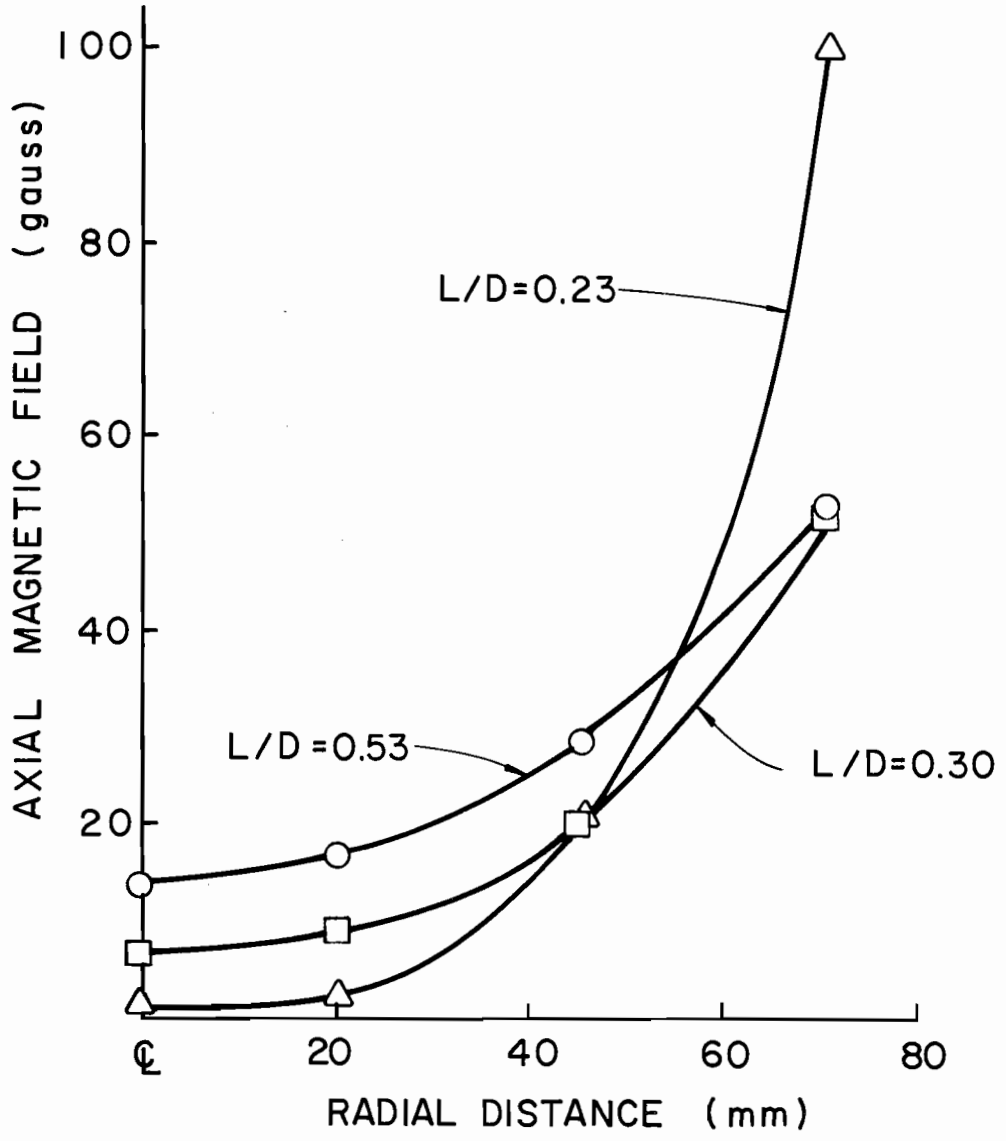


Figure 24. Cusped magnetic field thruster magnetic field variation.

magnet pole piece and anode. This complication prompted the development of a quantitative procedure for defining the ion production volume in an arbitrary discharge chamber design. The method developed for defining the boundary of the ion production volume consists of the following steps: (1) The plasma properties, as determined by Langmuir probe measurements, are used to calculate the ionization collision frequency at each probe location by use of Equation (8). The calculated collision frequencies are normalized with respect to the maximum value, and contours of the normalized collision frequencies are determined. (2) The single and double ion production rates are calculated for the entire discharge chamber volume. The collision frequency contour which encloses a large fraction (e.g., 95 percent) of the total single or double ion production rate is then used as the ion production region boundary. Once the boundary has been identified, volume-averaged values for the discharge chamber plasma properties can be calculated. These volume-averaged properties are useful for comparing the various discharge chamber configurations and explaining the thruster performance characteristics. As a part of this investigation, a computer routine was developed to perform the analysis described above. The program was written to be compatible with the ion production and volume-averaging programs of Peters and Wilbur [29] and calls these programs as subroutines. Input to the program consists of the discharge chamber geometry, Langmuir probe positions, plasma properties, and the specified fraction of the total ion production that the final contour line should enclose. The program output consists of a graphical display of the discharge chamber geometry and collision frequency contours, as well as the ion production region boundary. An example of the collision

frequency contours and ion production region boundary determined by the program is presented for a divergent magnetic field geometry in Figure 25 and for a cusped magnetic field geometry in Figure 26. In these figures the solid lines represent the normalized collision frequency contours, and the broken line represents the ion production region boundary. The inner, or highest, contour is for a normalized collision frequency of 0.9, and the contour line increment is 0.1. For the examples shown the ion production region boundary was defined as the collision frequency contour which enclosed 95 percent of the total single ion production rate.

The procedure described above for identifying the ion production region boundary has been quite useful in the following respects: (1) This method of identifying the important region for ion production resulted in much better agreement between calculated and measured quantities, such as propellant utilization and double-to-single ion density ratio, than had been realized when the ion production region boundary was identified using iron filings maps. (2) The collision frequency contours identify fundamental differences between the cusped and divergent magnetic field geometries. For example, the contour lines for the divergent magnetic field geometry are seen to diverge, much like the magnetic field lines. The contour lines for the cusped magnetic field geometry, on the other hand, clearly indicate a phenomenon that is not immediately obvious from considering magnetic field lines. The contour lines are drawn out towards the center magnet pole piece indicating a high energy density region extending radially outward from the center of the discharge chamber. (3) The ion production region boundaries clearly indicate the increase in the depth of the ion

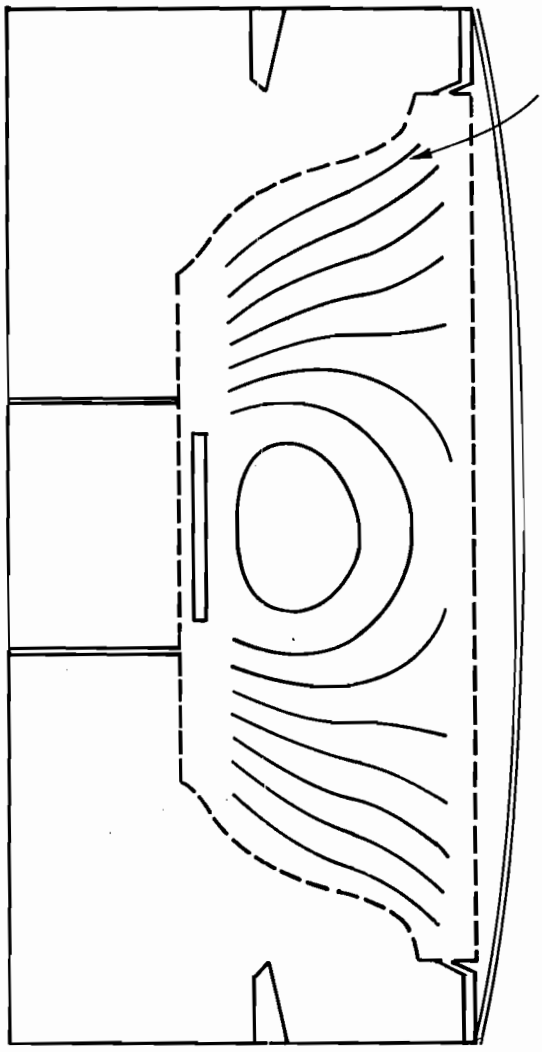


Figure 25. Collision frequency contours and ion production region boundary (divergent magnetic field geometry, L/D = 0.30). Collision frequency contour increment = 0.1.

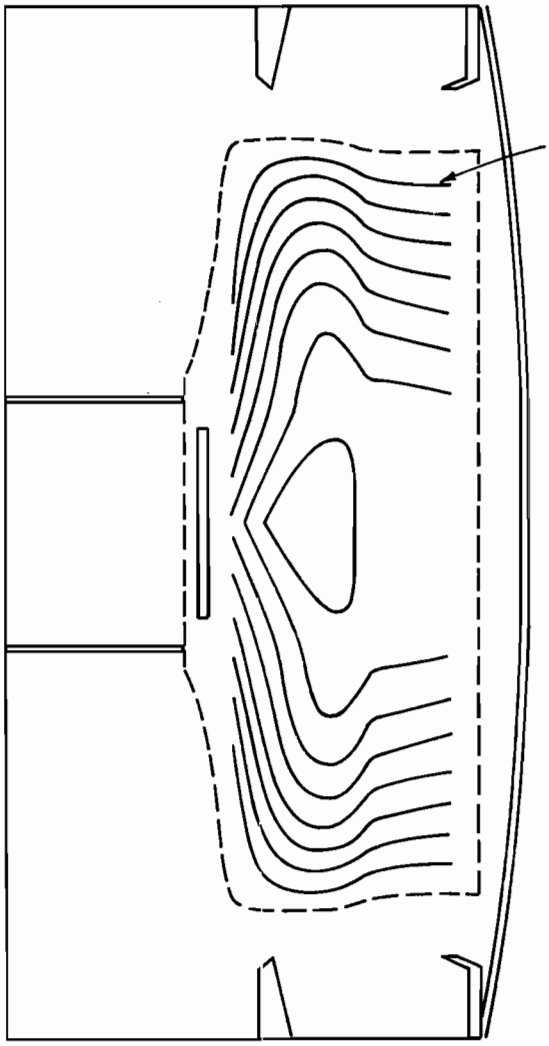


——— NORMALIZED COLLISION FREQUENCY CONTOUR

---- ION PRODUCTION REGION BOUNDARY

Figure 26. Collision frequency contours and ion production region boundary (cusped magnetic field geometry, L/D = 0.30). Collision frequency contour increment = 0.1.

production region near the chamber boundary which was realized with the cusped magnetic field geometry.

The shape of the contour lines in the cusped magnetic field configuration result in a T-shaped ion production region. This phenomenon is due to the existence of a "magnetic bottle" in the region between the cathode and center magnet pole pieces which can be visualized by considering the iron filings map of Figure 10a. Electrons injected through the baffle aperture tend to follow field lines which terminate on the center magnet pole piece. However, as the electrons approach the pole many are reflected by the strong magnetic field which exists there. As the reflected electrons approach the cathode pole piece many are reflected by the strong magnetic field in this region. This trapping effect is particularly evident in Figure 27 which shows the contours for the cusped field discharge chamber having a length equal to the SERT II thruster length. Contours for the same discharge chamber but a divergent magnetic field geometry are presented in Figure 28. Comparison of Figures 27 and 28 illustrates the dramatic change in the ion production region geometry caused by the change in magnetic field geometry.

Although the cusped magnetic field geometry generally resulted in a more uniform beam profile than the divergent field geometry, the discharge chamber having a length-to-diameter ratio of 0.53 was an exception to this rule. Figures 27 and 28 indicate why the divergent field geometry resulted in a more uniform beam profile than the cusped magnetic field geometry for this particular chamber length. The divergent field geometry has the region of high ion production located

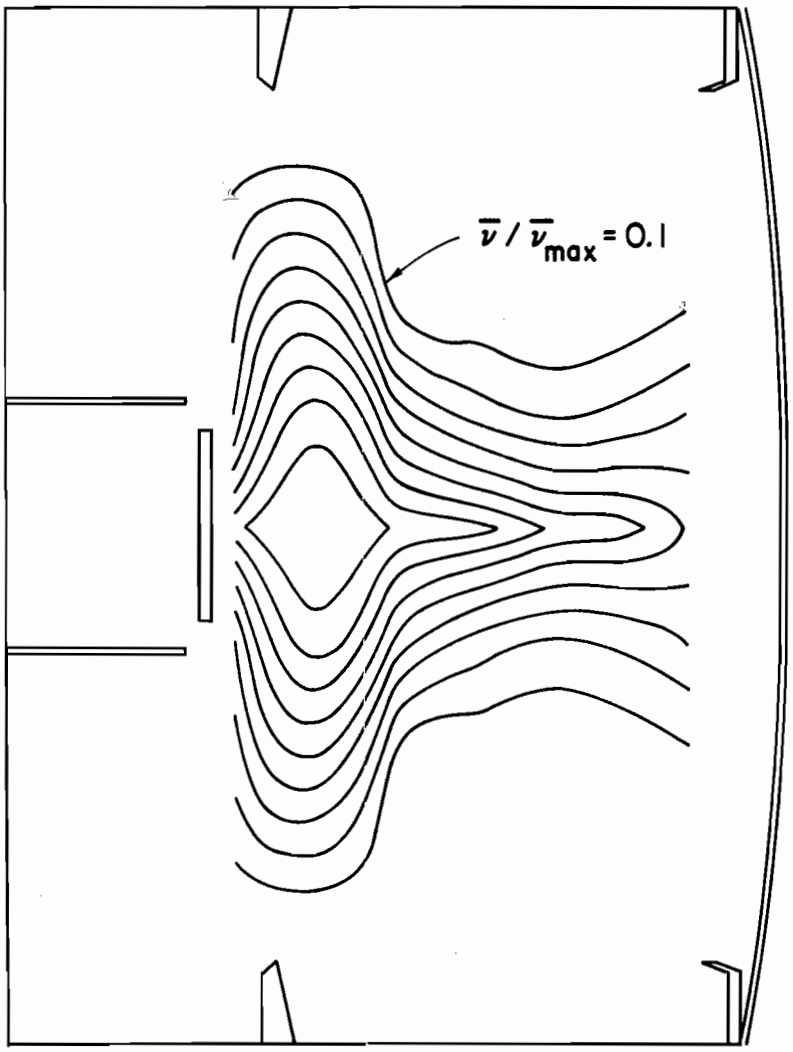


Figure 27. Collision frequency contours (cusped magnetic field geometry, L/D = 0.53). Collision frequency contour increment = 0.1.

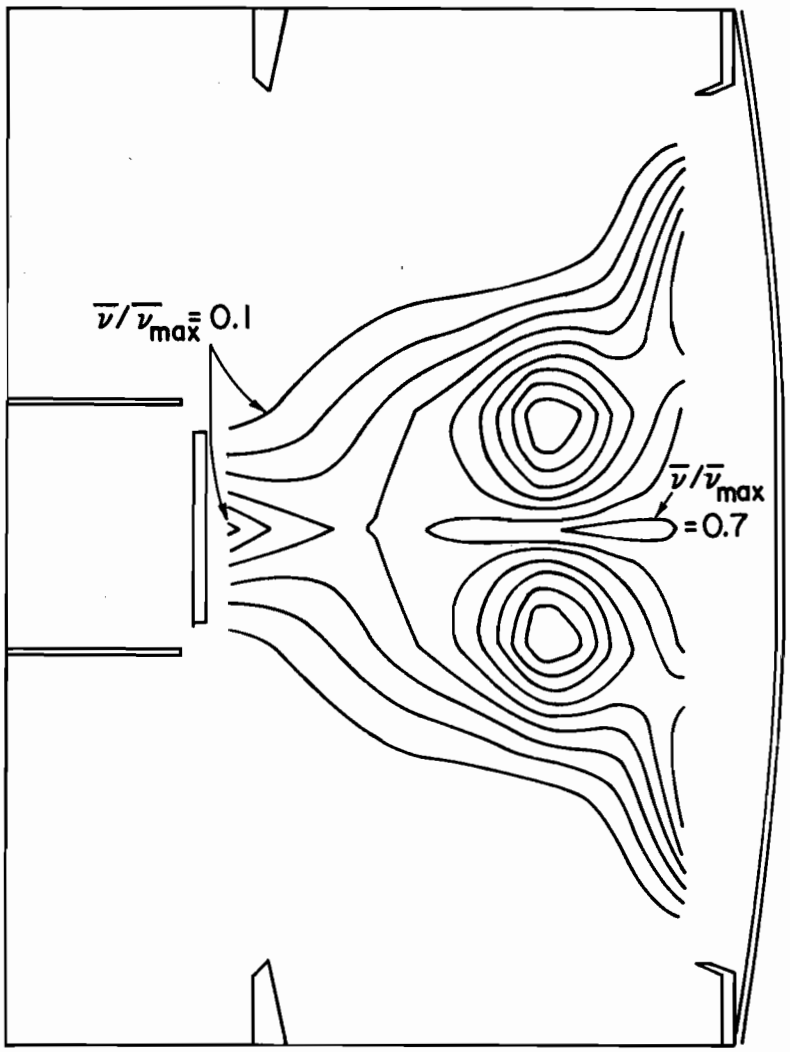


Figure 28. Collision frequency contours (divergent magnetic field geometry, L/D = 0.53). Collision frequency contour increment = 0.1.

near the screen grid, and the ion production region is spread out over a greater fraction of the chamber cross section.

The improvement in the beam profile uniformity which resulted from discharge chamber length reductions was discussed earlier in the chapter. The reason for the flatter profile was identified as an improvement in the uniformity of the plasma density profile near the screen grid, and this was attributed to a reduction in the magnetic field penetration into the discharge chamber. The collision frequency contours of Figures 26 and 27 illustrate this effect quite vividly. The contours in the downstream end of the cusped field discharge chamber have about the same shape as the magnetic field lines in this region, and a comparison of Figures 26 and 27 illustrates the radial expansion of the ion production region which accompanied the reduction in magnetic field fringing.

## Plasma Properties

The thruster operating conditions and volume-averaged plasma properties are presented in Table 2 for the twelve basic discharge chamber configurations (two magnetic field geometries and two upstream anode positions for each of the three discharge chamber lengths investigated). The thruster input power is seen to be about the same for each configuration. The operating condition which varied is the beam current, or propellant utilization, which was affected most by the discharge chamber length and upstream anode position. Table 2 also presents the single and double ion collision frequencies and the normalized densities and production rate fractions for each atomic and ionic species. These quantities were calculated using the computer routines described by Peters and Wilbur [29]. The normalized densities

# TABLE 2

## THRUSTER OPERATING CONDITIONS, VOLUME-AVERAGED PLASMA PROPERTIES, AND CALCULATED ION PRODUCTION FRACTIONS

| LENGTH-TO-DIAMETER RATIO | 0.23 | | | | 0.30 | | | | 0.53 | | | |
|---|---|---|---|---|---|---|---|---|---|---|---|---|
| MAGNETIC FIELD GEOMETRY | CUSPED | | DIVERGENT | | CUSPED | | DIVERGENT | | CUSPED | | DIVERGENT | |
| ANODE POSITION | UPSTREAM | DOWNSTREAM | UPSTREAM | DOWNSTREAM | UPSTREAM | DOWNSTREAM | UPSTREAM | DOWNSTREAM | UPSTREAM | DOWNSTREAM | UPSTREAM | DOWNSTREAM |
| THRUSTER OPERATING CONDITIONS | | | | | | | | | | | | |
| ANODE CURRENT (A) | 4.2 | 4.2 | 4.1 | 4.1 | 4.3 | 4.3 | 4.2 | 4.2 | 4.3 | 4.3 | 4.2 | 4.3 |
| ANODE POTENTIAL (V) | 36.8 | 37.7 | 35.1 | 34.7 | 36.7 | 36.2 | 36.5 | 34.2 | 37.0 | 37.0 | 37.0 | 37.0 |
| BEAM CURRENT (mA) | 611 | 452 | 600 | 484 | 625 | 462 | 582 | 519 | 514 | 442 | 522 | 477 |
| PROPELLANT FLOW RATE (mA) | 717 | 717 | 730 | 726 | 730 | 727 | 719 | 741 | 737 | 725 | 721 | 726 |
| VOLUME-AVERAGED PLASMA PROPERTIES | | | | | | | | | | | | |
| VOLUME-TO-AREA RATIO (cm) | 1.27 | 1.28 | 1.29 | 1.16 | 1.42 | 1.37 | 1.40 | 1.15 | 1.14 | 1.04 | 1.34 | 1.49 |
| MAXWELLIAN ELEC. TEMPERATURE (eV) | 4.8 | 3.0 | 5.0 | 3.5 | 4.8 | 3.2 | 5.9 | 3.6 | 3.0 | 3.0 | 3.3 | 3.2 |
| PRIMARY ELECTRON ENERGY (eV) | 30.2 | 27.4 | 29.0 | 27.2 | 27.9 | 26.6 | 29.4 | 26.1 | 21.7 | 23.2 | 27.2 | 19.3 |
| PRIMARY ELEC. DENSITY X $10^{-10}$ ($cm^{-3}$) | 1.1 | 0.9 | 1.2 | 0.9 | 0.7 | 0.9 | 0.9 | 1.3 | 0.8 | 0.7 | 0.7 | 0.5 |
| MAXWELLIAN ELEC. DENS. X $10^{-10}$ ($cm^{-3}$) | 28.3 | 28.5 | 28.2 | 31.3 | 30.2 | 34.9 | 26.3 | 32.6 | 37.3 | 36.2 | 30.4 | 25.6 |
| ION DENSITY X $10^{-10}$ ($cm^{-3}$) | 29.4 | 29.4 | 29.4 | 32.2 | 30.9 | 35.8 | 27.2 | 33.9 | 38.1 | 36.9 | 31.1 | 26.1 |
| NORMALIZED DENSITIES | | | | | | | | | | | | |
| GROUND STATE ATOMS | .460 | .480 | .463 | .456 | .451 | .440 | .482 | .457 | .442 | .457 | .459 | .484 |
| METASTABLE ATOMS | .116 | .155 | .112 | .149 | .128 | .162 | .103 | .142 | .170 | .167 | .163 | .185 |
| RESONANCE ATOMS | .332 | .307 | .323 | .329 | .305 | .314 | .285 | .315 | .320 | .315 | .305 | .251 |
| SINGLE IONS | .082 | .052 | .090 | .059 | .098 | .072 | .111 | .076 | .059 | .053 | .064 | .067 |
| METASTABLE IONS | .008 | .005 | .010 | .006 | .015 | .011 | .015 | .009 | .008 | .007 | .008 | .013 |
| DOUBLE IONS | .002 | .001 | .002 | .001 | .003 | .001 | .004 | .001 | .001 | .001 | .001 | .000 |
| SINGLE ION PRODUCTION FRACTIONS | | | | | | | | | | | | |
| GROUND STATE ATOMS | .314 (.35) | .285 (.65) | .325 (.34) | .269 (.48) | .304 (.23) | .254 (.54) | .367 (.22) | .288 (.53) | .228 (.47) | .238 (.49) | .261 (.49) | .243 (.33) |
| METASTABLE ATOMS | .254 (.22) | .340 (.36) | .247 (.21) | .332 (.25) | .295 (.13) | .365 (.28) | .233 (.15) | .317 (.30) | .400 (.22) | .393 (.23) | .370 (.25) | .456 (.15) |
| RESONANCE ATOMS | .431 (.30) | .375 (.51) | .428 (.29) | .400 (.37) | .401 (.19) | .381 (.42) | .400 (.20) | .396 (.42) | .372 (.33) | .369 (.35) | .369 (.37) | .301 (.21) |
| DOUBLE ION PRODUCTION FRACTIONS | | | | | | | | | | | | |
| GROUND STATE ATOMS | .035 (.61) | .006 (.84) | .025 (.40) | .005 (.36) | .018 (.15) | .001 (.0) | .032 (.22) | .003 (.0) | .002 (.0) | .002 (.0) | .003 (.52) | .003 (.0) |
| METASTABLE ATOMS | .009 (.61) | .002 (.84) | .006 (.40) | .002 (.36) | .005 (.15) | .000 (.0) | .007 (.22) | .001 (.0) | .006 (.0) | .001 (.0) | .001 (.52) | .001 (.0) |
| RESONANCE ATOMS | .025 (.61) | .004 (.84) | .018 (.40) | .004 (.36) | .012 (.15) | .001 (.0) | .019 (.22) | .002 (.0) | .001 (.0) | .001 (.0) | .002 (.52) | .002 (.0) |
| SINGLE IONS | .898 (.54) | .960 (.90) | .917 (.51) | .962 (.76) | .922 (.39) | .961 (.83) | .899 (.33) | .966 (.78) | .986 (.8) | .981 (.81) | .958 (.79) | .978 (.46) |
| METASTABLE IONS | .034 (.68) | .028 (.96) | .034 (.61) | .028 (.86) | .043 (.47) | .038 (.91) | .042 (.40) | .028 (.84) | .010 (.62) | .015 (.78) | .036 (.89) | .016 (.10) |
| SINGLE ION COLL. FREQUENCY ($sec^{-1}$) | 7685 | 3378 | 8304 | 4549 | 7212 | 4348 | 9376 | 5481 | 3488 | 3288 | 3780 | 2381 |
| DOUBLE ION COLL. FREQUENCY ($sec^{-1}$) | 1732 | 758 | 1929 | 866 | 1396 | 821 | 2308 | 1154 | 530 | 519 | 679 | 180 |

Numbers in parentheses indicate the fraction of the production rate due to the primary electron group.

indicate that about 50 percent of the heavy particles are ground state atoms, 15 percent metastable atoms, and 30 percent resonance atoms. The remaining heavy particles are single, metastable, and doubly charged ions. The single ion production fractions indicate that about 30 percent of the single ions are produced from ground state atoms, 30 percent from metastable atoms, and 40 percent from resonance atoms. The double ion production fractions, on the other hand, show that about 95 percent of the doubly charged ions are produced as a result of electron interactions with singly charged ions. The number in parentheses adjacent to the production rate fractions indicates the fraction of the production rate due to the primary electron group.

The plasma properties and collision frequencies presented in Table 2 can be used to explain many of the experimental observations presented in Chapter V. For example, with the cusped magnetic field geometry (upstream anode position) the improvement in performance caused by the reduction in discharge chamber length is due to the substantial increase in the single ion collision frequency $\bar{\nu}$. The plasma properties indicate the electron temperature and energy were increased significantly when the discharge chamber length-to-diameter ratio was reduced from 0.53 to 0.3, and this more than doubled the value of the single ion collision frequency. Further reduction in the discharge chamber length produced a small increase in the primary electron energy and a corresponding increase in $\bar{\nu}$. Results similar to those described above are also evident when considering the effects of discharge chamber length reductions in the divergent magnetic field geometry. Here a substantial increase in the collision frequency accompanied the reduction in discharge chamber length-to-diameter ratio from 0.53 to 0.30.

The higher collision frequency is seen to be due primarily to an increase in the Maxwellian electron temperature and primary electron energy. A further reduction in the discharge chamber length produced a slight reduction in electron temperature and energy, and this lowered the single ion collision frequency. However, the ion density increased due to the reduced loss rate caused by the lower electron temperature, and this resulted in a slight increase in the beam current.

The double ionization collision frequencies listed in Table 2 can be used to explain the variation in the double-to-single ion current ratio presented in Figures 14 and 17. For example, the chamber length reductions are seen to result generally in an increase in the collision frequency due to the increase in electron temperature and energy. This observation agrees fairly well with the measured double-to-single ion current ratio trends presented in Figures 14 and 17. The downstream movement of the anode caused a substantial reduction in the collision frequency as a result of the reduction in the Maxwellian electron temperature and primary electron energy. This produced a substantial reduction in the double-to-single ion current ratio as illustrated in Figures 14 and 17.

The performance degradation and reduction in the double-to-single ion density ratio which accompanied the downstream movement of the anode was due to a substantial reduction in the collision frequencies $\bar{\nu}$ and $\nu_+^{++}$. This was caused by a significant drop in the Maxwellian electron temperature and a slight reduction in the primary electron energy. Figure 29 compares the Maxwellian electron temperature and primary electron energy for the two different anode positions and indicates the significant reduction in the Maxwellian electron

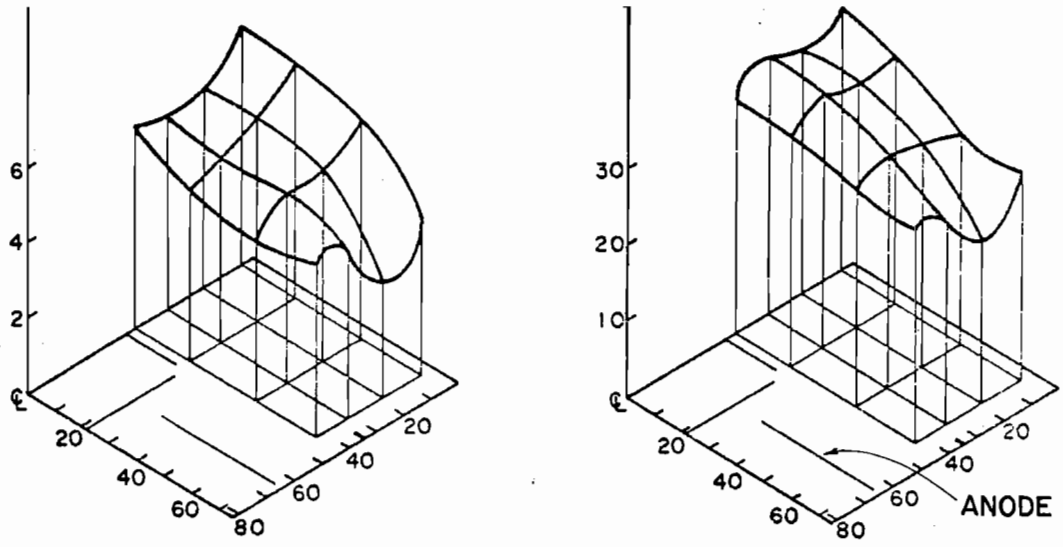


A. UPSTREAM ANODE POSITION

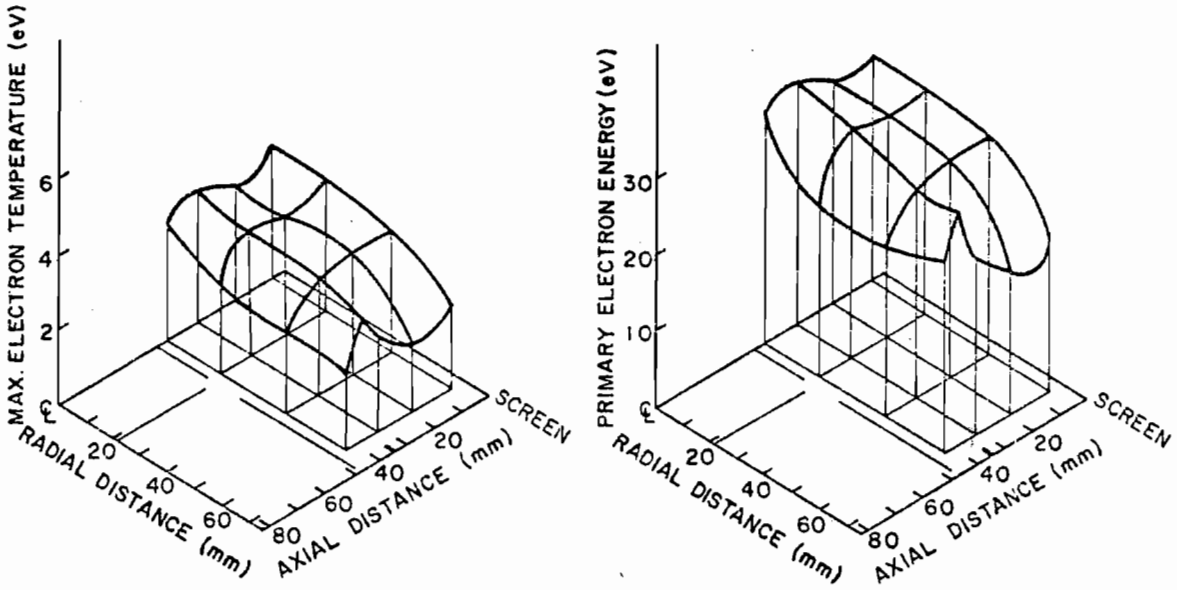


B. DOWNSTREAM ANODE POSITION

Figure 29. Effect of anode position on Maxwellian electron temperature and primary electron energy (cusped magnetic field geometry, L/D = 0.23). 730 mA propellant flow rate, 4 A anode current, 37 V anode potential.

temperature which resulted from the movement of the anode to the downstream position. The primary electron energy was also reduced, but the reduction is localized to the region close to the anode. An explanation for the reduction in electron temperature which resulted from the downstream anode movement can be given in the following manner. The electrons are trapped in a magnetic bottle region located a distance r from the upstream anode. Energetic electrons with a cyclotron radius greater than r will be collected by the anode and thus the maximum electron speed which can exist in this region is given by the cyclotron equation

$$V_{max} = \frac{qB}{m} r \tag{22}$$

where $V_{max}$ is the maximum electron speed, and qB/m is the electron cyclotron frequency. If a "maximum" speed is defined for the Maxwellian distribution function such that a large fraction (e.g., 99.99 percent) of the electrons have speeds less than this value, a relationship between $V_{max}$ and the electron temperature can be obtained

$$V_{max} = 3.2 \sqrt{\frac{2qT_m}{m}} \tag{23}$$

where q/m is the electron charge-to-mass ratio, and $T_m$ is the Maxwellian electron temperature. Equating the expressions for $V_{max}$ results in the following relationship between the electron temperature and the separation distance

$$T_m = 0.049 \frac{qB^2}{m} r^2 \qquad (24)$$

This expression indicates the strong dependence of the electron temperature on the separation distance r. The crude model leading to this result cannot be expected to be valid for all values of r, of course, since the expression was derived assuming the anode was the only factor which limits the electron temperature, and clearly this is not the case. What one would expect is that for large values of r the anode position has essentially no effect on electron temperature, but as the anode is moved closer to the field lines the temperature is significantly affected. This is just what was observed experimentally. The variation of beam current with anode position is presented in Figure 30 which shows that the anode was moved in the downstream direction for a considerable distance with essentially no effect on the thruster performance. Further downstream movement resulted in a sharp reduction in the beam current due to the electron temperature drop. Equation (24) can be used to estimate the anode position where the electron temperature and beam current should drop. Figure 29 shows that the electron temperature with the anode in the upstream position is about 4.4 eV. The magnetic field strength near the inner edge* of the circular upstream anode is about 15 gauss. Substituting these values into Equation (24) results in a value of r equal to 1.5 cm. This agrees fairly well with the results of Figure 30 which indicates a rapid drop in the beam current at about this anode position. With the anode in the downstream

*The inner edge was used since current measurements using a segmented upstream anode indicate about 99 percent of the current to this electrode is drawn by the inner segment.

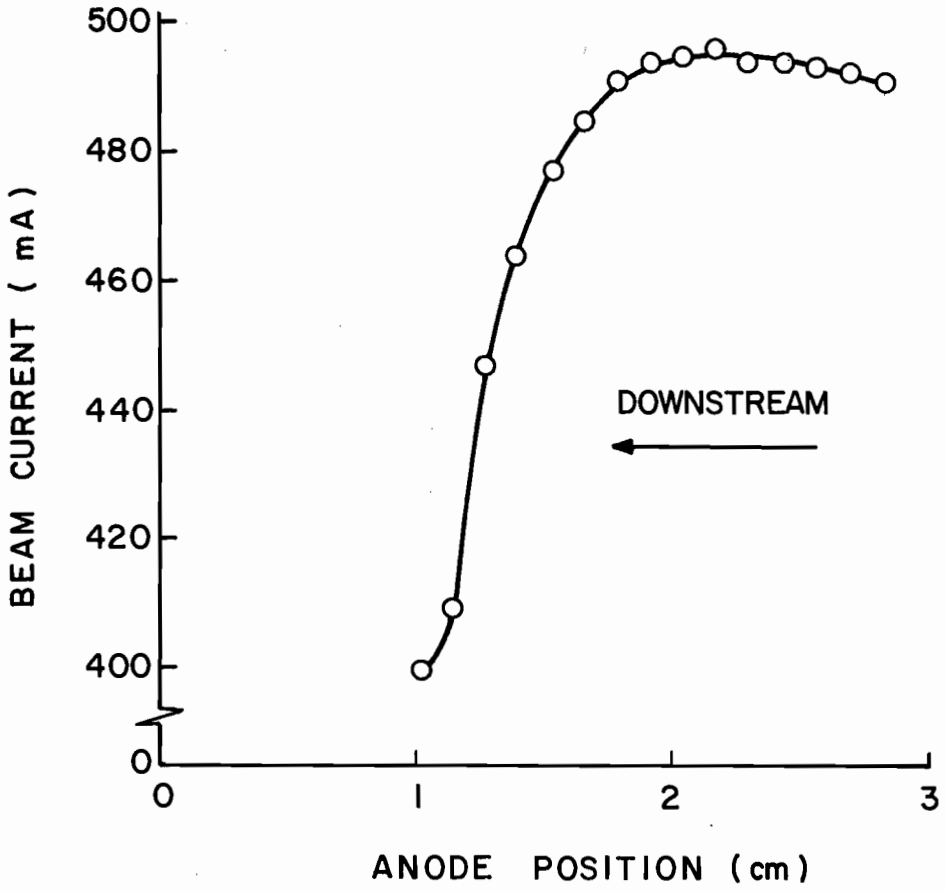


Figure 30. Variation of beam current with anode position (cusped magnetic field geometry, L/D = 0.23).

position r is approximately 1 cm, and evaluating Equation (24) results in a 2.2 eV electron temperature. This value agrees quite well with the downstream anode position results of Figure 29.

## Performance

The analysis of Chapter II suggested the discharge chamber modification illustrated in Figure 7b would result in a more uniform ion beam profile with improved performance characteristics and fewer double ions as compared with the configuration of Figure 7a. The performance and double ion predictions were based on the assumptions of a cylindrical ion production region and constant plasma properties, and these predictions generally proved to be valid in spite of the fact that the ion production region is not cylindrical and the plasma properties varied. As a result of the plasma property variations, the plasma ion production cost $C_i$ is not a constant. Therefore, the discharge power losses cannot be compared with the predictions of Chapter II since the plasma ion production cost is unknown. However, the propellant utilization and double-to-single ion density ratio can be calculated by use of the expressions developed in Chapter II and then compared with the measured values of these quantities. The calculations were made using Equations (14) and (19) which were derived assuming uniform plasma properties exist within the ion production region. The fact that the plasma properties in actual thrusters have a spatial variation was accounted for by introducing an equivalent uniform property region which has the same volume as the nonuniform property region. Average plasma properties were defined for the equivalent region such that the average values yield the same ion production rate as obtained by integrating the ion

production rate per unit volume over the nonuniform property region. The area of the uniform property region was reduced such that the ion loss rates calculated using the uniform plasma property values were the same as the loss rates calculated by integrating the measured ion flux rate over the boundary of the ion production region. A detailed description of the procedure used to calculate the volume-averaged plasma properties and the plasma nonuniformity factors used to reduce the area of the ion production region is given by Peters and Wilbur [29]. The results of the propellant utilization calculations are presented in Figure 31 which shows good agreement between the calculated and measured values. The calculated and measured values of the double-to-single ion density ratio are presented in Figure 32, and the agreement is considered reasonable. The scatter in the data is of the same order reported by other investigators [29].

## Radial Field Thruster

The radial field thruster configuration, which represents the limiting case of zero length-to-diameter ratio, was found to have a nonuniform beam profile and poor propellant utilization. The reason for this is evident by considering Figure 33 which shows the beam current density profile and an iron filings map of the magnetic field geometry. The iron filings map shows that the field lines leaving the baffle aperture region intercept the screen grid at a small fraction of the thruster radius. This results in the confinement of the high-energy electrons to a relatively small fraction of the chamber cross section much like the early axial field thrusters. In fact, the beam profiles

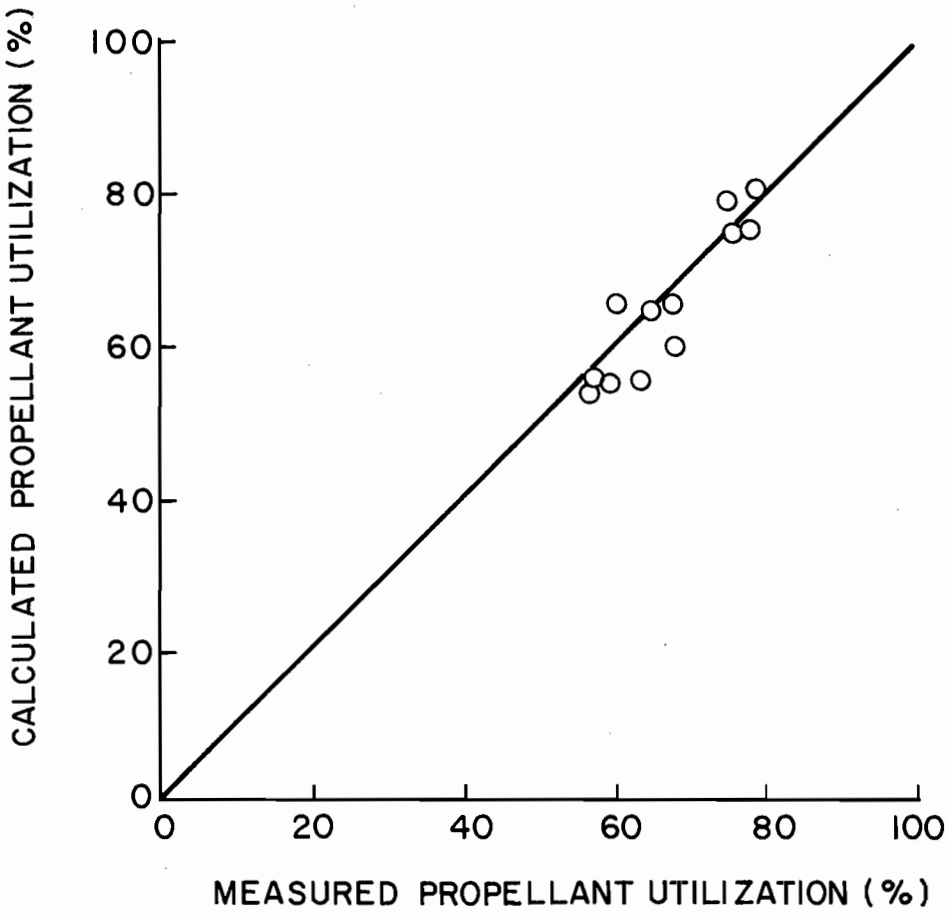


Figure 31. Comparison of calculated and measured propellant utilization.

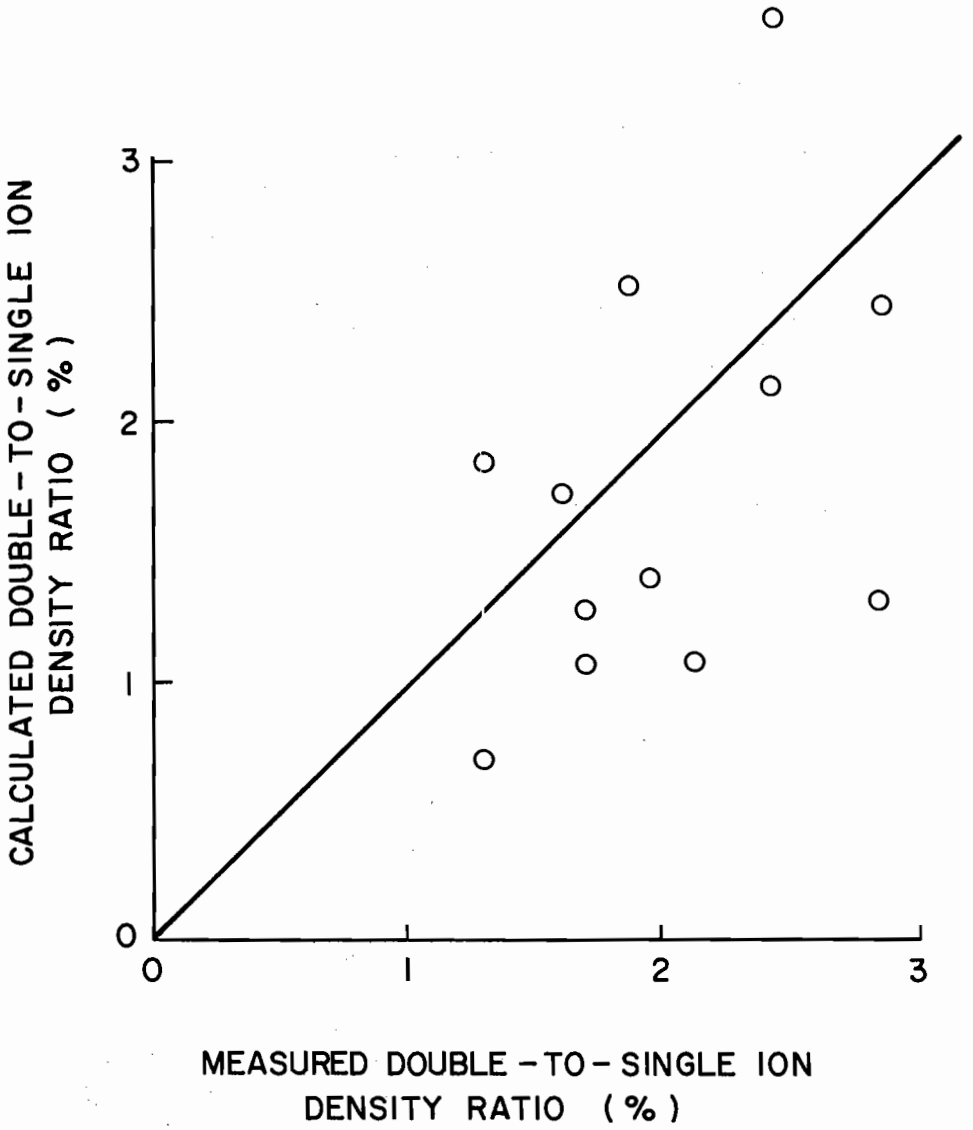


Figure 32. Comparison of calculated and measured double-to-single ion density ratio.

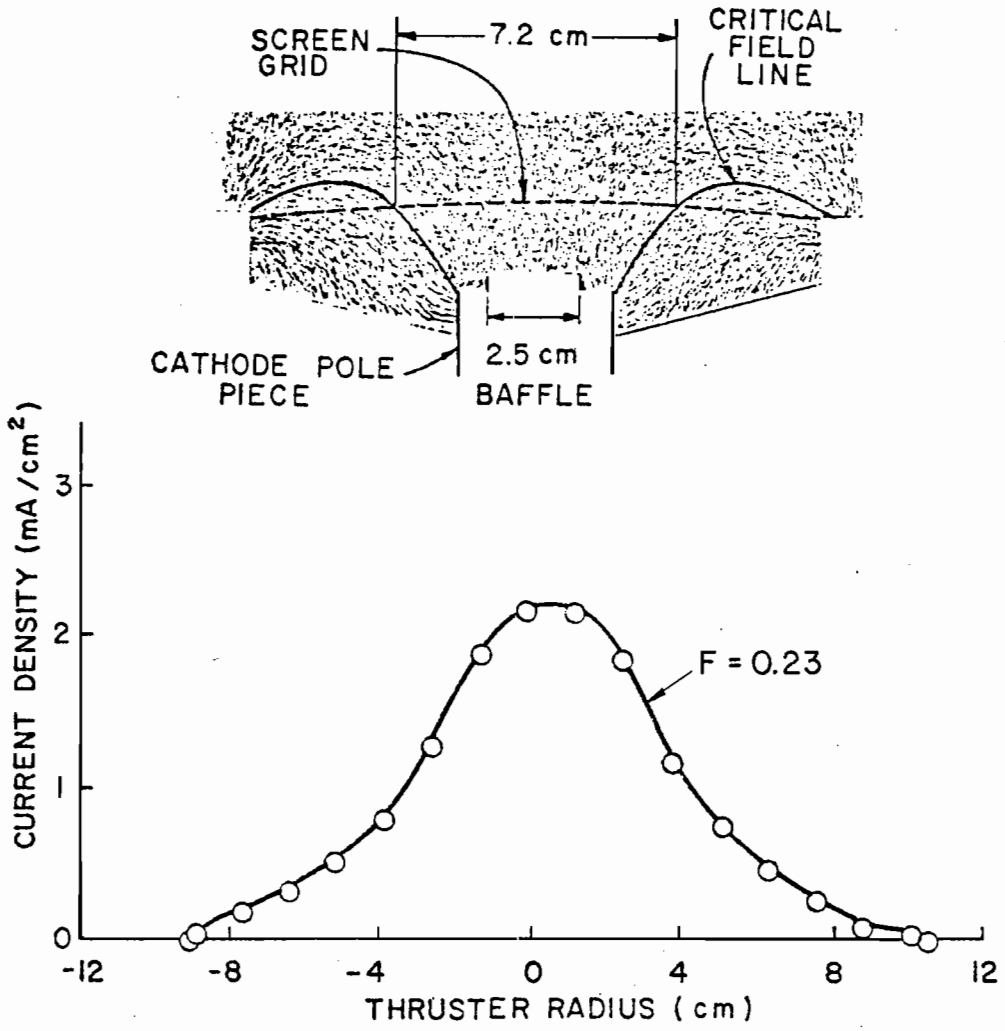


Figure 33. Radial magnetic field thruster beam current density profile and iron filings map (small baffle). 492 mA propellant flow rate, 3.3 A anode current, 37 V anode potential.

of the two thrusters are quite similar (e.g., Figures 5a and 33). With the high-energy electrons concentrated near the chamber centerline, the bulk of the ionization occurs in this region and neutrals outside this central core are not likely to become ionized. This results in a highly nonuniform beam profile and poor propellant utilization. Expanding the ion production region radially by moving the field line-screen grid interception point should result in a more uniform beam profile and improved propellant utilization. Figure 34 shows the results of shifting the field line interception point to about three-fourths of the chamber radius. Expanding the primary electron region volume to cover a greater fraction of the chamber cross section resulted in a 30 percent increase in the beam flatness parameter and a 26 percent increase in maximum propellant utilization.

Further improvements in the beam profile flatness and maximum propellant utilization were realized with the radial field thruster configuration by eliminating the field line-screen grid interception. This was accomplished by moving the accelerator system downstream as illustrated in Figure 35. This modification allowed the high-energy electrons access to the entire chamber cross section and resulted in a much more uniform beam profile. At the same input power conditions the beam flatness parameter and maximum propellant utilization were increased by a factor of two as a result of expanding the ion production region.

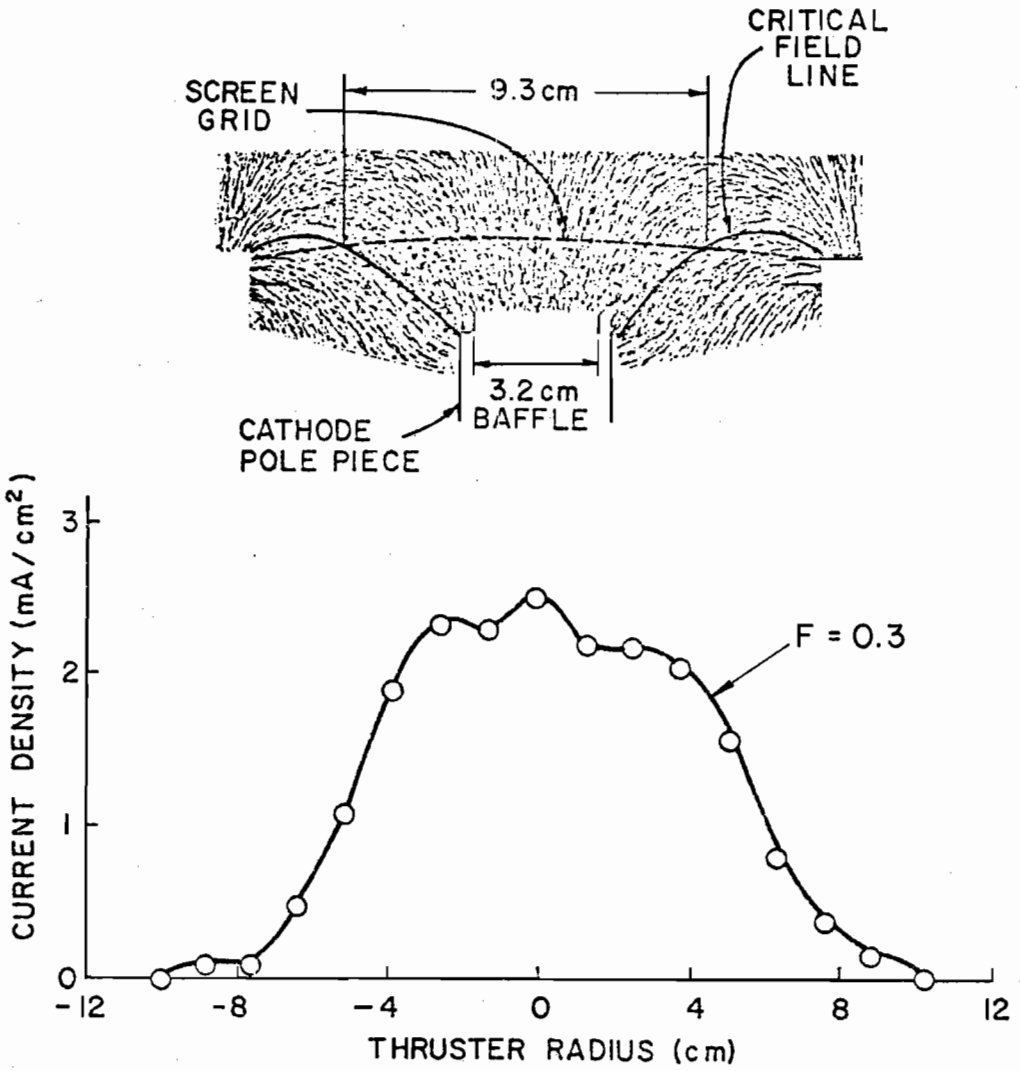


Figure 34. Radial magnetic field thruster beam current density profile and iron filings map (large baffle). 593 mA propellant flow rate, 5 A anode current, 37 V anode potential.

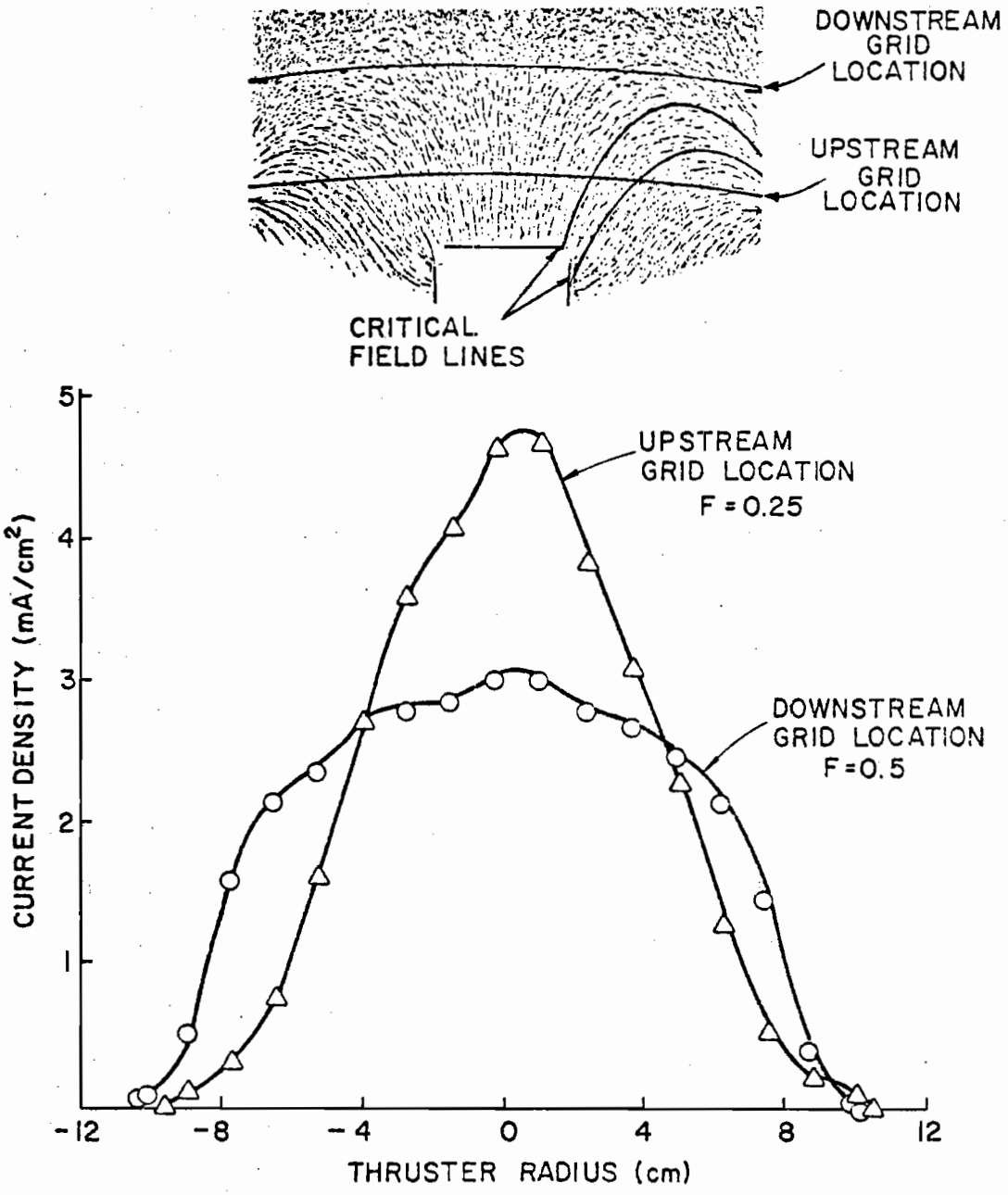


Figure 35. Radial magnetic field thruster iron filings map and the effect of grid location on beam current density profile. 750 mA propellant flow rate, 5 A anode current, 37 V anode potential.

## CONCLUSIONS

The most significant results of this investigation are as follows:

1. The cusped magnetic field discharge chamber design resulted in a 40 percent increase in the flatness parameters of both the ion beam current density profile and the double ion beam profile of the SERT II thruster. Based on the reductions in the maximum single and double ion current density, the improvement in beam profile uniformity should result in about a 40 percent increase in the accelerator system lifetime of this thruster. The anticipated lifetime improvement is due to a reduction in the charge-exchange ion erosion of the accelerator grid and reduced sputtering of the screen grid caused by the impingement of doubly charged ions.
2. The performance degradation which accompanied the improved beam profile uniformity is relatively small; a 7 percent increase in the discharge power loss and a 4 percent reduction in the propellant utilization of the SERT II thruster.
3. Analysis of discharge chamber performance and double ionization phenomena indicated that, along with the cusped magnetic field modification to the SERT II thruster, the discharge chamber length should be reduced. Chamber length reductions were found to result in a discharge power loss reduction of 100 eV/ion,

and an optimum chamber length was found. Both of these experimental results are in agreement with the predictions based on the analysis.

4. A quantitative procedure was developed and used for defining the ion production region boundary and was successful in verifying the critical field line concept of divergent field thrusters. Better agreement between theoretical calculations and experimental measurements of propellant utilization and double-to-single ion density ratio was realized using the boundary defined in this manner as opposed to a definition based on iron filings maps.
5. The collision frequency contours indicate a fundamental difference between the cusped and divergent magnetic field geometries. The cusped magnetic field configuration tends to trap energetic electrons in a magnetic bottle region in the upstream end of the discharge chamber. This phenomenon gives rise to a T-shaped ion production region in contrast to the bell shape of the divergent magnetic field configuration.
6. The axial position of the upstream anode was found to have a considerable effect on the thruster performance and double-to-single ion density ratio. Plasma property measurements indicated the performance degradation and reduction in double-to-single ion density ratio associated with a downstream movement of the anode was due primarily to a substantial reduction in the Maxwellian electron temperature.
7. The limiting case of a zero length-to-diameter ratio for both the cusped and divergent magnetic field geometries was

investigated, and the performance and beam profile flatness were seriously degraded with this geometry. The source of the problem was identified as the confinement of energetic electrons to the region close to the chamber centerline, and this was shown to be due to the magnetic field lines intercepting the screen grid. These observations identified an important design consideration. Discharge chambers should be designed so that the magnetic field lines originating in the baffle aperture region do not intercept the screen grid.

## REFERENCES


1. Stuhlinger, E., *Ion Propulsion for Spaceflight*, McGraw-Hill, New York, 1964.

2. Jahn, R. G., *Physics of Electric Propulsion*, McGraw-Hill, New York, 1968.

3. Kaufman, H. R., "An Ion Rocket with an Electron-Bombardment Ion Source," TN D-585, Jan. 1961, NASA.

4. Kaufman, H. R. and Reader, P. D., "Experimental Performance of Ion Rockets Employing Electron-Bombardment Ion Sources," American Rocket Society Paper 1374-60.

5. Clark, K. E., "Survey of Electric Propulsion Capability," *Journal of Spacecraft and Rockets*, Vol. 12, No. 11, Nov. 1975, pp. 641-654.

6. Kaufman, H. R., "Ion-Thruster Propellant Utilization," Ph.D. Thesis, June 1971, Dept. of Mechanical Engineering, Colorado State University, Fort Collins, Colo.

7. Kaufman, H. R., "Technology of Electron-Bombardment Ion Thrusters," *Advances in Electronics and Electron Physics*, Vol. 36, ed. L. Marton, Academic Press, New York, 1974, pp. 265-373.

8. Brewer, G. R., *Ion Propulsion Technology and Applications*, Gordon and Breach, New York, 1970.

9. Hudson, W. R. and Banks, B. A., "An 8-cm Electron Bombardment Thruster for Auxiliary Propulsion," AIAA Paper 73-1131, Lake Tahoe, Nev., Oct. 1973.

10. Hyman, J. and Poeschel, R. L., "Satellite Control Mercury Ion Thruster," AIAA Paper 73-1132, Lake Tahoe, Nev., Oct. 1973.

11. Kerslake, W. R., Goldman, R. G., and Nieberding, W. C., "SERT II: Mission, Thruster Performance, and In-Flight Thrust Measurements," *Journal of Spacecraft and Rockets*, Vol. 8, No. 3, March 1971, pp. 213-224.

12. Nakanishi, S. and Finke, R. C., "A 9700-Hour Durability Test of a 5-cm-diam Ion Thruster," AIAA Paper 73-1111, Lake Tahoe, Nev., Oct. 1973.

13. Collett, C. R., "A 7700 Hour Endurance Test of a 30-cm Kaufman Thruster," AIAA Paper 75-366, New Orleans, La., March 1975.

14. Vahrenkamp, R., "An Experimental Investigation of Multiple Ion Processes in Mercury Bombardment Thrusters," AIAA Paper 75-397, New Orleans, La., March 1975.

15. Wintucky, E. G., "A 20,000-Hour Endurance Test of a Structurally and Thermally Integrated 5-cm Diameter Ion Thruster Main Cathode," AIAA Paper 75-368, New Orleans, La., March 1975.

16. Wilbur, P. J., "Correlation of Ion and Beam Current Densities in Kaufman Thrusters," *Journal of Spacecraft and Rockets*, Vol. 10, No. 9, Sept. 1973, pp. 623-624.

17. Knauer, W., Poeschel, R. L., and Ward, J. W., "Radial Field Kaufman Thruster," *Journal of Spacecraft and Rockets*, Vol. 7, No. 3, March 1970, pp. 248-251.

18. Masek, T. D., "Plasma Properties and Performance of Mercury Ion Thrusters," *AIAA Journal*, Vol. 9, No. 2, Feb. 1971, pp. 205-212.

19. Kaufman, H. R. and Cohen, A. J., "Maximum Propellant Utilization In An Electron-Bombardment Thruster," *Proceedings of the Symposium on Ion Sources and Formation of Ion Beams*, Brookhaven National Laboratory, Upton, New York, Oct. 1971, pp. 61-68.

20. Bechtel, R. T., "Discharge Chamber Optimization of the SERT II Thruster," *Journal of Spacecraft and Rockets*, Vol. 5, No. 7, July 1968, pp. 795-800.

21. Masek, T. D., "Plasma Properties and Performance of Mercury Ion Thrusters," AIAA Paper 69-256, Williamsburg, Va., March 1969.

22. Wilbur, P. J., "15 cm Mercury Ion Thruster Research--1975," CR-134905, Dec. 1975, Colorado State University, Fort Collins, Colo.

23. Poeschel, R. L. and Knauer, W., "A Variable Magnetic Baffle for Hollow Cathode Thrusters," AIAA Paper 70-175, New York, N.Y., Jan. 1970.

24. Wilbur, P. J., "An Experimental Investigation of a Hollow Cathode Discharge," CR-121038, Dec. 1972, Colorado State University, Fort Collins, Colo.

25. Vahrenkamp, R. P., "Measurement of Double Charged Ions in the Beam of a 30-cm Mercury Bombardment Thruster," AIAA Paper 73-1057, Lake Tahoe, Nev., Oct. 1973.

26. Free, B. A., "Economic Tradeoff for Electric Propulsion Missions on Communications Satellites," AIAA Paper 71-683, Salt Lake City, Utah, June 1971.

27. Wilbur, P. J., Monthly Letter to W. R. Kerslake, Contract Monitor, NASA Grant No. NGR-06-002-112, Feb. 5, 1973.

28. Beattie, J. R., "Numerical Procedure for Analyzing Langmuir Probe Data," *AIAA Journal*, Vol. 13, No. 7, July 1975, pp. 950-952.

29. Peters, R. R. and Wilbur, P. J., "Double Ion Production in Mercury Thrusters," CR-135019, April, 1976, Colorado State University, Fort Collins, Colo.